

INFLUENCE OF MICROSTRUCTURE ON FRIABILITY
OF ALUMINA-ZIRCONIA ABRASIVES

By

ROBERT EUGENE SHEPLER

A DISSERTATION PRESENTED TO THE GRADUATE COUNCIL OF
THE UNIVERSITY OF FLORIDA
IN PARTIAL FULFILLMENT OF THE REQUIREMENTS FOR THE
DEGREE OF DOCTOR OF PHILOSOPHY

UNIVERSITY OF FLORIDA

1975

ACKNOWLEDGMENTS

The author wishes to thank the following:

Dr. E. Dow Whitney, supervisory committee chairman, for introducing the author to the field of hard materials and abrasives.

Dr. Robert T. DeHoff, supervisory committee member, for introducing the author to quantitative stereology and for discussions in its relation to the present work.

Drs. L. L. Hench, R. E. Loehman and J. B. Conklin, Jr., for serving on the supervisory committee.

Dr. V. M. Wald, 3M Company, for supplying sample materials and results of his toughness tests.

Dr. L. M. Zsolnay, Carborundum Company, for friability tests performed on the DeBeers Friatester.

Mr. E. J. Jenkins, for technical assistance with the scanning electron microscope; Mr. S. M. Gehl, for helpful discussions on quantitative stereology; and Mr. Richard Kennedy, for moral support and assistance after working hours.

Materials Science and Engineering Department of the University of Florida, for providing a graduate assistantship.

National Science Foundation, for financial support of the project leading to this dissertation.

TABLE OF CONTENTS

	Page
ACKNOWLEDGMENTS	ii
ABSTRACT	v
INTRODUCTION	1
Abrasives	1
Quantitative Microscopy	4
Alumina-Zirconia	10
Fracture and Toughness	21
EXPERIMENTAL PROCEDURE	23
Sample Preparation	23
Microhardness Measurements	25
Friability Measurements	25
Quantitative Microscopy Measurements	29
X-ray Diffraction	33
Density	33
Computer	33
RESULTS	34
Microhardness	34
Microstructural Characterization	34
Microstructural Control	38
Friability	81
Microstructural Control of Friability	81
Impurity Control of Friability	104
Density	121
X-ray	125
DISCUSSION	129
Microhardness	129
Microstructure	132
Zirconia Stabilization	144
Impurities	145
Friability and Grain Shape	147
CONCLUSIONS	148
FUTURE WORK	150

TABLE OF CONTENTS - Continued

	Page
REFERENCES	151
BIOGRAPHICAL SKETCH	155

Abstract of Dissertation Presented to the Graduate Council
of the University of Florida in Partial Fulfillment of the
Requirements for the Degree of Doctor of Philosophy

INFLUENCE OF MICROSTRUCTURE ON FRIABILITY
OF ALUMINA-ZIRCONIA ABRASIVES

by

Robert Eugene Shepler

June, 1975

Chairman: Dr. E. Dow Whitney

Major Department: Materials Science and Engineering

Counting measurements and mathematical relations of quantitative stereology have been used to characterize the geometric aspects of the microstructure of cast alumina-zirconia abrasives. The microstructure was controlled by varying processing parameters. The quench rate of the material from the melt was found to be the processing parameter exhibiting the most important control over the microstructure. Friability of the alumina-zirconia abrasives was measured using three methods: a ball mill test, the DeBeers friatest and the microfriability test developed for this study. Friability was found to be controlled by the geometric aspects of the microstructure. Two cases of microstructural dependence were studied: the eutectic composition case and compositions on the alumina side of the eutectic composition. For both cases one microstructural parameter, a scale factor, was found to control the friability. A fracture mechanics approach has been employed to explain the observed increase in strength

and toughness in the alumina-zirconia materials studied. The effects of impurities and the amount of stabilized zirconia were also examined to find their effects on the microstructure and the friability. Impurities can affect the friability beyond the extent associated with purely microstructural changes.

INTRODUCTION

It has been shown repeatedly how the microstructure of most any material affects its mechanical properties. A wealth of information for metals in this regard exists in the literature. Much of this information is also available for ceramics with more being realized continuously. The manufacturing of abrasives has been going on for many years but relatively little fundamental work has been done in relation to other areas of ceramics. It is the purpose of this study to show the relation between the geometric microstructure of the alumina-zirconia abrasive and its mechanical properties.

Abrasives

It is rather difficult to select suitable abrasive grains for the grinding of various materials, owing to the many kinds of abrasive grains available and to the lack of a basic understanding of their mechanical properties. In many cases today, selection methods used are based on the know-how obtained from past experiences.

Accurate and scientific descriptions and the subsequent improvement of the processes of grinding with abrasives has received considerable attention. At the same time there have been developed new hard materials for use in these processes. One of the major blocks to technological progress is the lack

of connection between parameters describing the material and parameters describing the process. This missing connection is the characterization of the material of interest. Characterization is a knowledge of the relevant details of the atomic structure and composition of the material. It includes translating the materials properties into fundamental characteristics, chemistry, structure and texture.

Hard materials used in abrasive grinding have many uses in other areas. Generally, the physical and chemical properties of these materials are quite well known. The process of grinding requires optimum use of certain of these basic properties.

Much work has been done trying to model the grinding process. Varying degrees of success have been attained using single grain models. Tests on single grains have been useful in developing these models. A means is needed to relate single grain tests and basic properties. Microstructural characterization provides this means. This study uses microstructural characterization to relate material properties to single grain properties and particularly to friability.

Friability is perhaps the only property which is always specified for an abrasive material. Even though the grinding process is very complex and the abrasive-workpiece combination adds to this complexity, friability remains the most general parameter. Friability is the measure of the extent of an abrasive material to break down, to fracture, upon

impact. Friability is sometimes reported as toughness where toughness is the inverse of friability.

The toughest abrasive grain, hence the least friable, is not always the desired material for a grinding operation. On the contrary, different grinding methods are typed generally according to the friability of the abrasive. Light duty, precision and finish grinding all use a friable grain. The grain breaks down rapidly so new sharp grains are constantly being exposed on the cutting surface. This is especially important in precision and finish grinding. Heavy duty stock removal requires very tough grains. For this type of operation it is desired to maximize the amount of material removed by grinding compared to the amount of abrasive removed.

The grinding ratio is a measure of the material removal rate in a grinding operation. It is the ratio of the amount of material removed to the amount of grinding media removed. High grinding ratios mean a longer abrasive life. But just as for friability, the highest grinding ratio is not always suited to a particular grinding operation. For heavy duty stock removal, high grinding ratios are desired, the objective being metal removal and not precision or surface integrity. Friability and grinding ratio are related even though grinding ratio measurements are influenced by the type of abrasive grain bonding. High grinding ratios are obtained using abrasives of low friability.

Quantitative Microscopy

All materials whether they be metals, ceramics or cermets have an internal structure. The electronic structure relates to electron distributions in a perfect crystal. The atomic arrangement structure reports the periodic aspects and crystal defects. The geometric microstructure is the arrangement of grains and amorphous states. Finally, the geometric macrostructure determines the shape of the total body of material. All of these structural aspects determine the chemical, physical and mechanical properties of the body.

Interest will be focused here on the geometric microstructure and its controlling influence on the mechanical properties of an abrasive grain. If indeed the geometric microstructure does control mechanical properties, then it will be of practical importance to determine how to control the microstructure.

In order to quantitatively relate the above-mentioned aspects, a method of quantitatively measuring and quantitatively describing the geometric microstructure is needed. The techniques and relations of quantitative microscopy, or quantitative stereology, provide this means. These techniques and relations provide for quantitative estimates of geometric properties of three-dimensional structures from quantitative measurements on two-dimensional sections of that structure [1,2]. This involves purely geometric relationships which will not be derived or justified here, only presented and used.

Three counting techniques were employed in this study which give estimates of three independent geometric features: volume, surface area and surface curvature.

The point counting technique permits the estimation of volume fraction. The count is made on a representative two-dimensional section of the structure to be studied. Figure 1a schematically represents such a section. The point count is made by randomly placing a set of points on the section and counting those that lie on a feature of interest, e.g., on the dark phase. It has been shown that a regular array of points provides the best estimate (smallest statistical error) [3]. In Figure 1b the test points are defined by the intersection of the lines forming the grid. The ratio of the number of points lying in the dark phase to the total number of points is P_p , the point fraction. P_p provides an unbiased estimate of V_v , the volume fraction of the dark phase:

$$P_p = V_v \quad (1)$$

Volume fraction has no units, being a measure of volume per volume, cm^3/cm^3 .

A line intercept count can be made with the same grid used for the point count in Figure 1b. A line count is made by randomly placing a test line on a representative two-dimensional section and counting the number of times the line intercepts a feature of interest. The grid in Figure 1b is randomly placed so the lines forming the grid can be used as test probes for the line intercept count. If the feature of

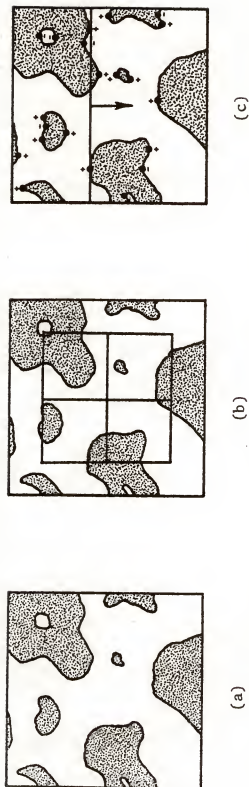


Figure 1. Illustration of counting techniques: (a) random representative plane section of two-dimensional material, (b) counting grid for P_p and N_L counts on plane section, (c) sweeping tangent line count.

interest was the phase boundary between the light and dark phase, then a count of the number of intersections per unit length yields the line intercept count, N_L . The line intercept count provides an unbiased estimate of the total surface area per unit volume [4] between the dark and the light phase:

$$N_L = \frac{1}{2} S_V \quad (2)$$

S_V has units of cm^{-1} being a measure of area per volume, cm^2/cm^3 .

A sweeping tangent line count can also be made on a two-dimensional section. This count is illustrated in Figure 1c. A line is moved normally across the plane section and the number of tangents it makes per area of the section with the lineal feature of interest on the two-dimensional plane is counted. Positive or negative tangent counts are formed depending on whether the tangent is formed with an element of positive or negative curvature. The definition of which is positive and which is negative is arbitrary and can be defined according to convenience. In the case of Figure 1c, if a positive count is one where the dark phase is on the concave side of the curved interface at the tangent formation, then the number and sign of the counts are as illustrated. The sweeping tangent line count, T_A , thus performed gives an unbiased estimate of the total surface curvature per unit volume [5], M_V , of the light phase-dark phase interface:

$$M_V = \pi T_A \quad (3)$$

where $T_A = T_A^+ - T_A^-$, T_A^+ is the number of positive tangent counts and T_A^- is the number of negative counts. M_V has units of cm^{-2} being a measure of curvature per volume, cm/cm^3 .

Another property that can be obtained from the sweeping tangent line count is the total absolute surface curvature, $|M_V|$, which is estimated by

$$|M_V| = \pi(T_A^+ + T_A^-) \quad (4)$$

While M_V and $|M_V|$ are not completely independent, they yield different parameters of geometric description which together may provide a better description of some microstructures.

Average properties can be computed from the previously mentioned global properties. The mean phase intercept [6], $\bar{\lambda}$, is such an average property. It can be obtained from

$$\bar{\lambda} = 4 V_V / S_V \quad (5)$$

The mean phase intercept has units of length. For the system of Figure 1 and the counts previously made, this would provide a measure of the mean phase intercept of the dark phase. This parameter can be used as a scale factor since it is a measure of size.

Another average property is the average mean surface curvature, \bar{H} . Surface curvature is defined in terms of the two principal normal curvatures, κ_1 and κ_2 , at any point on a surface. The mean surface curvature, H , is the average of these two quantities

$$H = \frac{1}{2} (\kappa_1 + \kappa_2) \quad (6)$$

In the general case, H varies from point to point on the surface. It can be shown [5,7] that the average value of H is given by

$$\bar{H} = \frac{M_V}{S_V} = \frac{\pi T_A}{2N_L} \quad (7)$$

\bar{H} will have the units of reciprocal length, e.g., cm^{-1} . So from the counting methods mentioned, an estimation of the average mean surface curvature can be obtained.

A final parameter of interest is the product of the mean phase intercept and the average mean surface curvature, $\bar{\lambda}\bar{H}$. It is dimensionless and combines the information obtained from all three counting techniques mentioned:

$$\bar{\lambda}\bar{H} = \frac{4V_V M_V}{S_V^2} = \frac{\pi P_P T_A}{N_L^2} \quad (8)$$

The relations and techniques presented in this section may be applied to structures of arbitrary geometry; their validity requires only that a representative sample of the structure be sampled uniformly. No simplifying geometric assumptions about the structure are necessary. The field of quantitative stereology contains other counting techniques and relations but the ones presented here are the only ones used in this study. Also, the two-phase system of Figure 1 used to explain the techniques does not show all the general features of an arbitrary two-phase system but only shows those most closely related to this study.

Microstructural analysis as performed above is a statistical measurement. The common standard deviation applied to this set of data will yield the number of readings (grid placements) required to achieve any predetermined accuracy.

Alumina-Zirconia

The commercial uses of the alumina-zirconia system are mainly in the abrasive and refractory industries. Alper [8,9] has pointed out its importance as a refractory brick for glass tanks. For use as an abrasive, alumina-zirconia has proven to be superior in snagging and billet conditioning operations by Pahlitzsch and Thormahlen [10] and by Coes [11]. Its superiority in floorstand grinding has been shown by Erikson and Gibb [12]. In all cases the superiority comes from larger metal removal rates at faster grinding speeds; large grinding ratios are obtained.

Many attempts have been used to employ single grain tests to predict behavior of abrasive wheels. These tests have seen varying degrees of success with more recent models giving good correlations. On the basis of single grain tests, Matsuo and Oshima [13] and Shaw and others [14-16] have shown the alumina-zirconia grain to be superior under certain conditions and to give poorer performance under others.

The alumina-zirconia system was the first multi-phased system to see appreciable commercial development. Other multi-phase systems are being explored now but none have been developed yet except as single point cutting tools. The high

strength of the alumina-zirconia grain is attributed to its two-phase structure.

Alumina-zirconia forms a simple binary eutectic as is evident in the phase diagram of Figure 2 which is a slight modification of the one proposed by Alper [9]. Wartenburg and others [17,18] proposed a binary diagram as did Cevales [19]. Figure 2 reflects a eutectic temperature of 1870°C and a eutectic composition of 42 wt% ZrO_2 . Solid solutions on both sides of the diagram are very limited with maximums of generally no more than 1% reported.

The microstructure visible from a polish plane of a fusion cast eutectic composition is shown in Figure 3. The colony structure contains zirconia rods and plates imbedded in α -alumina grains. The eutectic grains grow along a three-fold symmetry axis of the α -alumina. By controlling the solidification parameters, growth rate and temperature gradient, and impurities, Schmid and Viechnicki [20] could produce either random or oriented eutectic microstructures.

Impurities have been shown to cause colony structure in metal systems [21] and they are probably the cause of the colony structure in the alumina-zirconia system. By using large temperature gradients and minimal thermal asymmetry, Schmid and Viechnicki [20] obtained homogeneous eutectic structures free of colonies. In this colony-free structure they no longer obtained a rod-type microstructure but exclusively a lamellar-type microstructure.

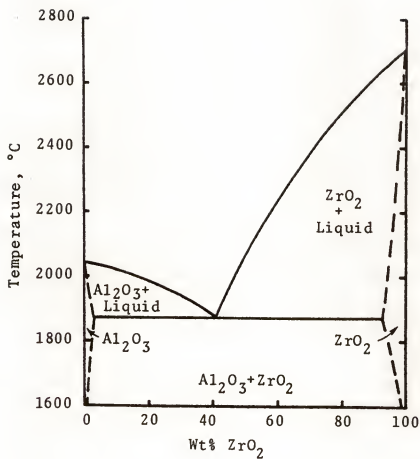
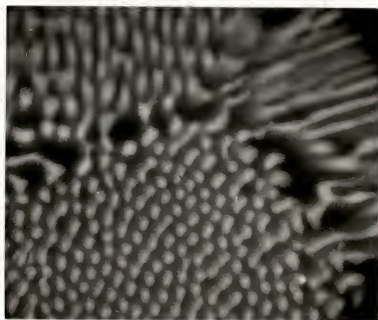


Figure 2. Phase diagram for alumina-zirconia system.



(a)

750X



(b)

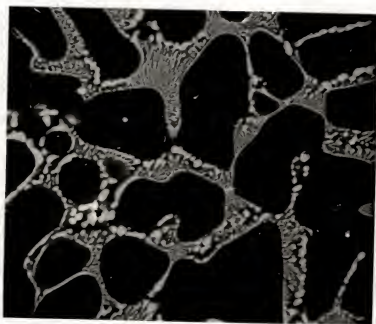
12,000X

Figure 3. Scanning electron micrograph of polish plane of fusion-cast eutectic composition alumina-zirconia.

For compositions between pure alumina and the eutectic composition, the microstructure obtained is shown in Figure 4. It consists of primary alumina dendrites in a supporting matrix. Figure 4 is from a fusion cast sample. On cooling, primary α -alumina dendritically freezes out until the eutectic temperature is reached. At the eutectic temperature the remaining liquid is of nearly the eutectic composition and a eutectic type solidification occurs similar to Figure 3. The dendritic nature of the primary α -alumina grains is not immediately apparent from Figure 4. Selected planes through more directionally solidified structures show it better and the view down a pore (shrinkage cavity) in Figure 5 makes the dendritic nature very obvious.

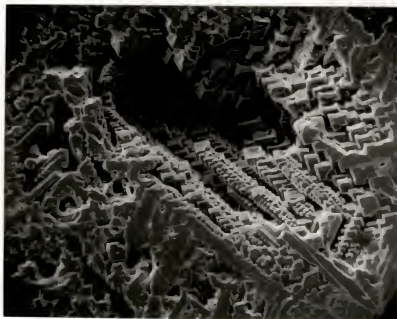
Compositions between the eutectic and pure zirconia have a structure as shown in Figure 6. There is primary zirconia in the supporting matrix. The primary zirconia frozen first on cooling from the melt can have an equigranular shape, Figure 6a, or a dendritic and needlelike shape, Figure 6b, depending on the composition and the degree of superheat in the liquid [9].

The primary alumina in the eutectic composition and all compositions on the alumina side of the eutectic serve to nucleate the eutectic microstructure. The primary zirconia for compositions on the zirconia side of the eutectic is surrounded by a ring of alumina. From the findings of Sundquist and Mondolfo [22], alumina is the first phase to nucleate



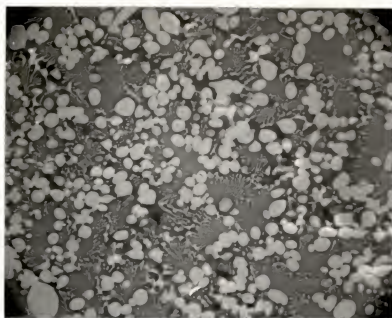
1200X

Figure 4. Scanning electron micrograph of polish plane of fusion-cast 25 wt% ZrO_2 -75 wt% Al_2O_3 .



600X

Figure 5. Scanning electron micrograph of 25 wt% ZrO_2 -75 wt% Al_2O_3 looking down a pore. Shows dendritic nature of primary alumina.



(a)

1300X



(b)

1350X

Figure 6. Scanning electron micrographs of fusion-cast 50 wt% ZrO_2 -50 wt% Al_2O_3 . (a) Equigranular primary ZrO_2 , (b) dendritic primary ZrO_2 .

and causes nucleation of zirconia when growth of the eutectic occurs.

The structures mentioned previously are all obtained by growth from the melt. Structures obtained by sintering alumina and zirconia powders below the melting temperature result in the alumina and zirconia crystals being separated. These types of structures were not investigated in this study since they are not of interest as an abrasive grain.

Most commercial abrasive grain compositions come from the alumina side of the eutectic or the eutectic composition itself. Compositions around 25 wt% ZrO_2 prove to yield the toughest grains. Materials are fusion cast to give the microstructures shown above.

The toughness of this grain is attributed to hard crystals of primary α -alumina being supported by a softer eutectic matrix. It is expected that the primary phase crystals are of higher modulus of elasticity than the eutectic matrix. Such a system conforms to findings determined for other composite structures which are characterized by high strength, for example glass fiber reinforced plastics [23].

An aspect of the alumina-zirconia system that has never been resolved to the satisfaction of this author is the question of the amount of alumina solid solution in zirconia and its effect on the phase morphology of the zirconia, i.e., does alumina stabilize zirconia in either the tetragonal or cubic phase modification? Zirconia normally occurs in the monoclinic state under ambient conditions. The phase

transformation monoclinic to tetragonal on heating and the reverse on cooling has been well documented [24]. The transformation tetragonal to cubic on further heating is not as well documented [24]. Many solid solutions of other materials with zirconia are known to stabilize zirconia in either the tetragonal or cubic phase at room temperature.

Zirconia suffers a destructive 7-9% volume increase in the tetragonal to monoclinic phase inversion which severely limits what otherwise could probably be the most useful high temperature oxide ceramic known. This accounts for the large amount of work and publications on controlling the phases of zirconia.

In fusion cast alumina-zirconia, the zirconia will have undergone the volume increase on cooling if it is in the monoclinic phase at room temperature. The zirconia is generally reported to be in the monoclinic phase with some workers reporting various amounts of the tetragonal or cubic phase stabilized. Schmid and Viechnicki [25] reported that only the monoclinic phase was present but suggest that a trace of a cubic peak could have been observed from their x-ray powder diffraction pattern. Even a small percentage of stabilized cubic zirconia in their samples could be explained by their relatively high impurity concentrations of CaO and MgO which both stabilize zirconia in the cubic modification. Andreeva [26] found no solid solution of Al_2O_3 in ZrO_2 but suggests that Al_2O_3 with the presence of Y_2O_3 does stabilize zirconia. Krauth and Meyer [27] found no solid solution or stabilization

for their slow cooled plasma jet cast alumina-zirconia. However, in their rapid quench experiments they report increasing amounts of tetragonal stabilized zirconia with increasing amounts of alumina up to total stabilization at 70 mole% ZrO_2 . Between 30 and 60 mole% ZrO_2 they reported finding only a glassy phase. They attribute the stabilized tetragonal zirconia not to solid solution by the alumina but to a crystallite size effect. Garvie [28] has found tetragonal stabilization due to a crystallite size effect in experiments on zirconia only. Bailey and others [29] also attribute their observed tetragonal stabilization in ball milled zirconia to a size effect. Hennicke and Vaupel [30] report tetragonal stabilization of zirconia by alumina. Their observations could be attributed to the size effect proposed by Garvie [28] and Krauth and Meyer [27] or maybe to an impurity effect; since their sample preparation techniques were quite different (precipitated hydroxides of ZrO_2 and Al_2O_3) and the fact that they measured solid solution of 1 mole% Al_2O_3 in ZrO_2 , they may have observed actual alumina stabilized zirconia.

Even though some stabilization of zirconia in the alumina-zirconia system has been reported, the zirconia is basically in the monoclinic modification at room temperature. Thus it has undergone the volume increase and since cracking is not observed even in very dense samples the structure must be strained. The zirconia probably experiences compressive forces while the alumina lattice is in tension.

Fracture and Toughness

Ceramics have traditionally been referred to as a class of materials which fail in a brittle manner. Once a crack is initiated, there is no resistance to propagation and catastrophic failure results. The increase in need to use ceramics in demanding mechanical and thermal stresses combined with high temperatures has been met mainly by trying to make stronger ceramics. Abrasive machining is one such demanding area. High mechanical stresses and temperatures approaching the melting temperature of the workpiece can be encountered at the abrasive grain-workpiece interface. Simply making stronger ceramics gives a higher fracture-initiation stress at failure. Once the fracture is initiated, the higher kinetic energy from stronger ceramics produces a fracture which is still catastrophic and even more spectacular. In these type ceramics failure occurs without warning.

If once past the stage of initiation the propagation of a crack could be arrested, then tough ceramics could be produced. Some amount of plastic deformation is thought to accompany crack propagation in all materials including ceramics [31-34]. Not all ceramics necessarily fail in a brittle manner when subjected to a load and do exhibit some degree of toughness. Gupta [31] has argued that stable crack propagation cannot occur in a single-phase homogeneous brittle material. However, in multiphase ceramics there is a distinct division in energy demand between various phases, so the stages of initiation and propagation are separate. The

presence of selective inhomogeneities in a ceramic material can prevent the premature growth of an unstable crack.

High values of fracture energies are generally accompanied by low values of strength. Gupta [31] attributes this discrepancy in multiphase systems to imperfect bonding between the dispersed phases and the matrix. The most promising materials from this standpoint appear to be the "self-generated" composites derived from the eutectics of mixed oxides.

EXPERIMENTAL PROCEDURE

Sample Preparation

Most samples used in this study were prepared by casting from the melt. Reagent grade powders of the individual constituents were weighed out and mixed. Alumina and zirconia from a number of commercial suppliers were used with no noticeable differences in resulting samples provided impurities were of relatively small trace amounts. Blending of the powders was done in a ball mill for 24 hrs. Blended powders were then cold pressed into pellets.

Some pellets were arc cast on a water cooled copper hearth plate. A tungsten electrode in an argon atmosphere was used. This method provided very fast quench rates -- from melt to about 600°C in 15 sec -- but samples were usually porous and had varying amounts of tungsten oxide contaminant since the electrode was slowly consumed. Since both alumina and zirconia are electrical nonconductors, small samples only, less than 2 gms, could be fabricated at one time using this method.

Other pellets were cast in a resistance heated furnace. The furnace had a tungsten heating element, tungsten heat shields and was operated in an argon atmosphere. Temperature was monitored with tungsten-tungsten rhenium thermocouples

and an optical pyrometer. Molybdenum crucibles were used. Quench rates up to 800°C/min were readily attainable using this furnace. Samples ranging from 5 to 30 gms were fabricated by this method.

Other samples used were obtained from commercial suppliers as bulk lumps or crushed and sized grains. These samples were all cast from the melt in electric arc furnaces. Various quenching methods were employed to include casting large ingots, pouring into thin slabs, pouring over steel balls, and sandwiching between steel plates to various thicknesses.

All samples were crushed in a hammer mill and sized using Tyler standard screen sieves. Random samplings of sized grains were picked for microstructural studies. These grains, usually four in number, were cold mounted in epoxy potting compound. They were then ground and polished using successively finer diamond grinding and polishing media. Some grinding was done with silicon carbide. Polishing was done through 1/4 micron diamond paste. Mounted samples were coated to give conducting surfaces for use in the scanning electron microscope. Coating was initially done with a gold-palladium alloy but later switched to carbon coating when this was found to give better phase contrast in the scanning electron microscope.

Microhardness Measurements

Microhardness numbers were obtained from samples cold mounted and polished as mentioned above. A Kentron microhardness tester was used with a Vickers indenter and loads of 100 and 1000 gms. Indenting velocity was approximately 0.01 cm/sec and the indenter remained in contact with the sample for approximately 10 sec. Microhardness numbers were also obtained using a Knoop indenter with loads of 100 gms.

Friability Measurements

Three methods of measuring friability have been employed: a ball mill test, the DeBeers friatester and a controlled impact test.

The ball mill test* results are reported as toughness numbers relative to an Al_2O_3 material standard. The mills were fabricated from 8 in OD 1/8 in wall steel tubing. The tube was cut to length (8 in) and covers were fitted to the ends. The rolling speed of the mill was 34 rpm. The impact media were cylindrical slugs 3/4 in diameter and 3/4 in long of fully hardened drill rod. Approximately 50 ml of material to be tested and 40 slugs (1780 gms) were used for each test. The slugs were weighed after each test and a 41st slug added when the total weight dropped to 1735 gms. When the total weight of the 41 slugs dropped to 1735 gms, the entire batch was discarded and replaced.

*Ball mill testing was done at 3M Company.

A narrow screen cut of material was used. The material and the slugs were put in the mill and the mill set into rotation on a conventional set of rollers including a rotation counter. Periodically the test was stopped and the material was sieved through a stack of four screens and the weight retained on each screen and in the pan was recorded. All material was then put back into the mill with the slugs and the test resumed. The test ended when most of the material was on the finest screen or the pan.

The selection of screens was arbitrary within limits. The coarsest screen was the first available screen finer than that of the starting material. The other three screens were selected to have approximately 70%, 40% and 20% of the opening of the coarsest screen.

The data after each screening were collected and reduced to give the number of rotations required to reach this condition with a standard Al_2O_3 material and quoted finally as relative toughness.

The DeBeers Friatester* is a vibrator capable of shaking cylindrical capsules in the direction of their axes at the frequency of 2400 ± 20 rpm with an amplitude of 0.325 ± 0.015 in. The capsules are carbon steel R_c 58-62 with 0.500 ± 0.005 in ID and 0.752 ± 0.006 in height in the cylindrical cavity when the capsule is closed. One cover of the capsule is flat and the other has a $9/32$ in concave radius. Each capsule has one

*Results from DeBeers Friatester were furnished by Carborundum Company.

hardened steel ball of 5/16 in diameter and 2.045 gm to 2.025 gm weight.

Material to be tested was a -30+40 wire screen cut. Between 0.39 and 0.41 gms were weighed into a capsule. The capsules were agitated for 15 sec. After this, the samples were rescreened through a #50 wire mesh screen. The percentage passing #50 mesh is considered destroyed. If the sum of the amount retained and the amount passed differed from the starting amount by more than 1%, the test was rejected. The differences actually observed were never more than 0.1%. Three tests were obtained for each sample and the median of the three results reported on the condition that none of the other two results deviate by more than 2% from the median. The friability is reported as the percent destroyed.

The controlled impact test or microfriability test consists of dropping a controlled weight from a controlled height onto an individual grain; see Figure 7. The grain rests between two tungsten carbide plates with the weight striking the upper plate and the bottom plate resting firmly on a massive piece of steel. Grains from a narrow sieve cut are tested one at a time, then resieved to give the microfriability as the percent destroyed. The majority of the tests were performed on a -10+14 US Standard sieve cut with the fraction passing a #18 sieve being the percent destroyed.

Approximately 1 gm of material was used for each microfriability test. Prior to actual testing a -7+18 sieve cut of material was tumbled for 24 hrs in a steel jar. The



(a)



(b)

Figure 7. Microfriability testing apparatus; (a) assembled, (b) tungsten-carbide chamber.

2.5 in diameter jars, Figure 8, were rotated at 22 rpm. The grains were then "tabled" prior to the microfriability test. Tabling consisted of rolling the grains down an inclined tube onto a tilted vibrating table, Figure 9. The idea being that the closer the grain was to a sphere, the farther it would roll down the table before falling off the edge. Grains used in the microfriability test were collected from the farther end -- "spherical end" -- of the table. The tabling was not perfect, with many grains remaining at the blockier end which, by visual inspection, appeared to belong more toward the spherical end. Fortunately, visual inspection showed nearly a complete absence of "flats" and "slivers" at the spherical end. So, the grains collected at the blockier end were run a total of four more times for each sample, giving any one grain a total of five chances to be accepted for further testing. The tumbling and tabling of the grains was done to minimize the effects of particle shape on the impact test. A large number of grains was actually tested per sample to statistically "iron out" the remaining particle size effects.

Quantitative Microscopy Measurements

The quantitative microscopy counting measurements were performed with the aid of a Cambridge Stereoscan scanning electron microscope. An optical microscope was tried but failed on two counts. In some cases, the features were too small to be resolvable in an optical microscope

Figure 8. Tumbling jars.



Figure 9. Vibrating table to eliminate flats and slivers.

(magnifications up to 70,000X were used) and in all cases poor phase contrast was obtained between the alumina and zirconia phases. Because of the high mass contrast between aluminum and zirconium, excellent phase contrast was obtained in the scanning electron microscope. The high contrast facilitated observations of the geometric features of interest.

Actual counting measurements were done at magnifications of 500X to 70,000X. A 25-point grid was used for the point fraction counts and 3 horizontal lines were used for the line intercept counts. Only horizontal lines were used to eliminate the uncertainty in vertical magnification due to tilting of the sample. Nearly all samples were counted with zero degree tilt angle but the 3 horizontal line convention was maintained. The counting grid was placed directly on the CRT and the counts made on the features observable there.

The sweeping tangent line count was made using a grid consisting of five small individual squares. The vertical raster line on the CRT was used as the sweeping test line and the tangent counts were made by visual observation in the areas defined by the five squares. Later the 25-point grid and the 5-square grid were combined so all desired measurements could be made from each screen placement on the sample.

A minimum of 50 grid placements was used in counting most samples. A very few samples were counted with 25 grid placements. The grid placements were made by moving the sample mechanically a random distance, then focusing and counting. Grid placements were rejected if they fell on

areas showing large cracks, large amounts of porosity or obvious polishing defects, i.e., grain pullout. Properly mounted and polished samples gave rise to very few, i.e., one or two, rejected grid placements per sample.

X-ray Diffraction

X-ray powder diffraction data were obtained with a Norelco diffractometer equipped with a graphite crystal diffracted beam monochromator. A copper target x-ray tube was used. Powder patterns were scanned at 0.5 and 1.0 deg/min. Peaks for zirconia phase analysis were scanned at 0.25 deg/min. Samples were mounted on glass slides using a collodion-amy1 acetate solution.

Area analysis of zirconia peaks for polymorph percentages was accomplished using a planimeter. Corrections were made for Lorentz polarization factors and the method of Garvie and Nicholson [35] used for percentage calculations.

Density

Density measurements were made using the wax impregnation-water suspension techniques. Sample sizes for these measurements varied from 0.2 gm to 5 gm.

Computer

Much of the data reduction was done on an IBM 360-165 computer.

RESULTS

Microhardness

Microhardness numbers for the alumina-zirconia system obtained with Vickers and Knoop indenters give similar results. Figure 10 shows the variation of diamond pyramid hardness numbers (Vickers indenter) with composition. A nearly linear relation exists. Figure 11 shows the results of the Knoop hardness tests. This also results in a nearly linear plot. The samples used in these tests varied by composition only. Other factors were held constant, i.e., they represent similar quench rates and the same fabrication procedure. These samples were cast in the arc melter so exact control of quench rates was not possible.

Similar results have been shown for the alumina-hafnia system [36].

Microstructural Characterization

The techniques of quantitative microscopy as described earlier have been used to characterize the microstructure of cast alumina-zirconia materials. The techniques have been applied in two separate cases, that of the eutectic composition and that for compositions on the alumina side of the eutectic composition.

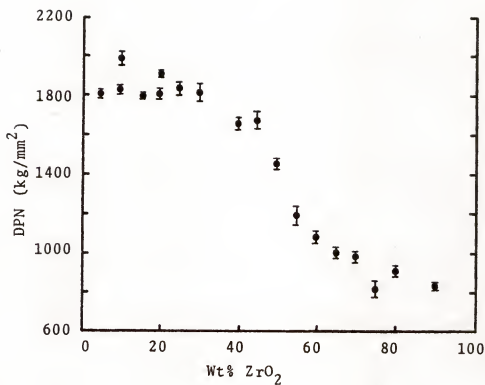


Figure 10. Diamond Pyramid Numbers (DPN) for arc-cast alumina-zirconia; 1000 gm load.

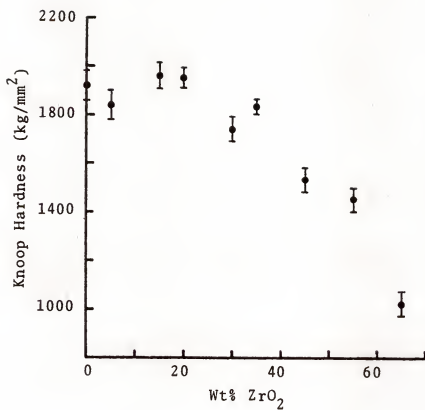


Figure 11. Knoop hardness for arc-cast alumina-zirconia; 100 gm load.

The first case where quantitative microscopy measurements were made was for samples with compositions between pure alumina and the eutectic composition. The volume fraction of the dendritically frozen primary alumina in the supporting matrix was measured, see Figure 4. Surface area and surface curvature counts were made on the interface between the primary alumina crystals and the supporting matrix. For notational purposes here, the primary alumina is called the α phase and the supporting matrix the β phase. The parameters examined were:

V_V^α = volume fraction of the α phase (primary alumina)

$S_V^{\alpha\beta}$ = total surface area per unit volume of the interface between the α and β phases (primary alumina-supporting matrix interface)

$M_V^{\alpha\beta}$ = total surface curvature per unit volume of the interface between the α and β phases

$\bar{\lambda}^\alpha$ = mean phase intercept of the α phase

$\bar{H}^{\alpha\beta}$ = average mean surface curvature of α - β interface.

The second case is for the eutectic composition which yields the two-phase structure shown in Figure 3. Volume fractions were calculated for the zirconia rods and plates and surface areas and surface curvatures of the alumina-zirconia interface. For notational purposes the zirconia phase was called the γ phase and the alumina phase called the ω phase. The notation used is explained below in the summary of the microstructural parameters investigated.

V_V^γ = volume fraction of the γ phase (zirconia)

$S_V^{\gamma\omega}$ = total surface area per unit volume of the interface between the γ and ω phases (zirconia-alumina interface)

$M_V^{\gamma\omega}$ = total surface curvature per unit volume of the interface between the γ and ω phases

$\bar{\lambda}^\gamma$ = mean phase intercept of the γ phase

$H_V^{\gamma\omega}$ = average mean surface curvature of the interface between the γ and ω phases.

Since all samples were nominally of the eutectic composition for the γ - ω measurements, V_V^γ would be expected to be constant from sample to sample. This was found to be the case with only minor variations probably due to small compositional differences and errors in white and black level determinations influencing the P_p^γ count. Figure 12 shows a range of $S_V^{\gamma\omega}$ and $M_V^{\gamma\omega}$ values encountered and a typical polish section for each of those values.

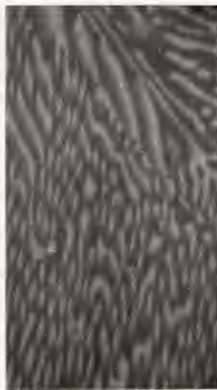
The two cases, α - β and γ - ω , measure different geometric aspects of the microstructure. The supporting matrix, β phase for α - β case, is essentially of the eutectic composition and has the same microstructural characteristics as the eutectic composition. Thus the β phase is actually the γ - ω case. Qualitative observation shows the size of the α phase dispersion to be at least an order of magnitude larger than the size of the γ phase dispersion.

Microstructural Control

There may be a number of ways to control the microstructure in any given material. One way to control it in the alumina-zirconia system is by varying the chemical composition. The effects of chemical composition on microstructure for compositions between pure alumina and the eutectic composition



$$S_V^{\gamma\omega} = 7.93 \times 10^4 \quad M_V^{\gamma\omega} = 1.06 \times 10^9$$



$$S_V^{\gamma\omega} = 4.17 \times 10^4 \quad M_V^{\gamma\omega} = 6.55 \times 10^8$$



$$S_V^{\gamma\omega} = 3.64 \times 10^4 \quad M_V^{\gamma\omega} = 6.07 \times 10^8$$



$$S_V^{\gamma\omega} = 1.16 \times 10^4 \quad M_V^{\gamma\omega} = 8.55 \times 10^7$$

Figure 12. Scanning electron micrographs of a range of $S_V^{\gamma\omega}$ and $M_V^{\gamma\omega}$ values encountered in eutectic composition alumina-zirconia; all micrographs are at 6500X.

are shown in Figures 13 through 15. These figures reflect data for arc melted samples.

Figure 13 shows V_V^α decreases from 1.0 to 0 as the amount of zirconia is increased. A monotonically decreasing curve is expected in order to be consistent with the phase diagram. The exact shape of this curve depends on other variables, especially the quench rate. Small differences in the curve can be obtained, making a compositional series of samples with a different quench rate. Thus the curve of Figure 13 is one curve out of a family of similar possible curves.

The variation of total surface area with composition is shown in Figure 14. The surface is that between the primary alumina crystals and the supporting matrix. At 0 wt% ZrO_2 only the alumina is present so $S_V^{\alpha\beta}$ is 0, and at 42 wt% ZrO_2 only the matrix phase is present so $S_V^{\alpha\beta}$ is 0. Between these two extremes the α - β interface exists so the curve goes through a maximum. Again this curve is but one curve of a family of possible curves, but of a larger range than in the V_V^α case. Great variation in $S_V^{\alpha\beta}$ for a given composition can be obtained as will be shown later.

The effect of composition on the total surface curvature is shown in Figure 15. As in the $S_V^{\alpha\beta}$ case, $M_V^{\alpha\beta}$ is 0 at 0 and 42 wt% ZrO_2 . Between these extremes, $M_V^{\alpha\beta}$ will have a maximum greater than zero and minimum less than zero, using the sign convention where the curvature of the α - β interface is considered positive if the α phase is on the concave side of the curved surface. For compositions slightly less than 42 wt%

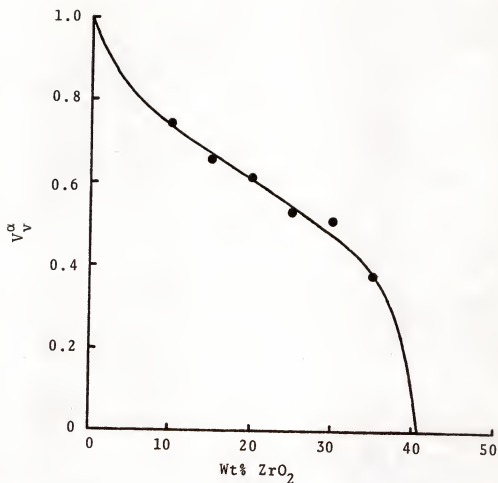


Figure 13. Volume fraction of primary alumina dendrites as a function of composition for arc-cast alumina-zirconia.

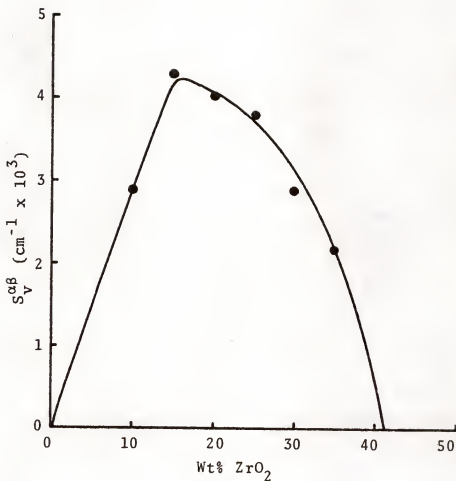


Figure 14. Total surface area per unit volume of primary alumina dendrites and supporting matrix interface as a function of composition for arc-cast alumina-zirconia.

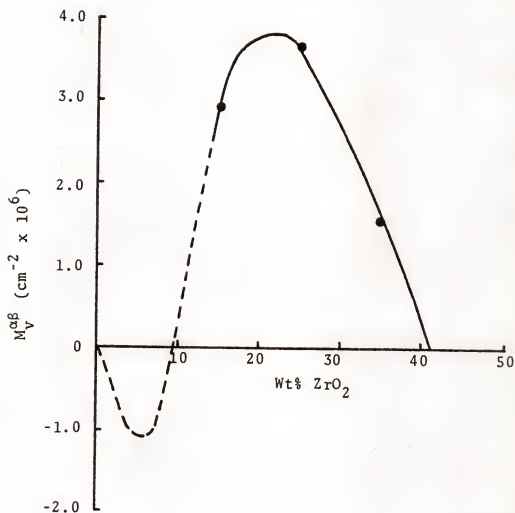


Figure 15. Total surface curvature per unit volume of primary alumina dendrite and supporting matrix interface as a function of composition for arc-cast alumina-zirconia.

ZrO_2 , the α phase will be the dispersed phase and thus $M_V^{\alpha\beta}$ will have positive values. For compositions slightly greater than 0 wt% ZrO_2 , the β phase will be the dispersed phase and $M_V^{\alpha\beta}$ will have negative values. Somewhere between, $M_V^{\alpha\beta}$ will go through zero. Since the α phase is the dendritically frozen primary alumina and the β phase is the last phase to freeze out (the eutectic composition), then it is qualitatively reasonable that the β phase will be continuous down to small wt% ZrO_2 values (regardless of the continuity of the α phase). Thus the crossover $M_V^{\alpha\beta}$ value of 0 should occur at small wt% ZrO_2 values and the data obtained support this conclusion. Insufficient data were obtained for the series of Figure 15 to pinpoint the wt% ZrO_2 value for the $M_V^{\alpha\beta}$ crossover. This crossover point and the exact shape of the curve are determined by other variables than the composition and thus the curve depicted is one of a family as in the two preceding cases.

For a given composition the microstructure can be controlled by the quench rate in cast samples. This appears to be the most influential factor controlling the microstructure for the compositions studied. This is shown qualitatively in Table I for the γ - ω case. The samples represented there were cast into slabs of various thicknesses where the thinner slabs provided faster quench rates. V_V^Y is essentially constant, $S_V^{\gamma\omega}$ increases with increasing quench rate and $M_V^{\gamma\omega}$ increases with increasing quench rate. The mean phase

Table I
Dependence of Microstructure on Quench Rate

Thickness	V_V^Y	$S_V^{Y\omega}$ (cm^{-1})	$M_V^{Y\omega}$ (cm^{-2})	$ M_V^{Y\omega} $ (cm^{-2})	$\bar{\lambda}^Y$ (cm)	$\bar{H}^{Y\omega}$ (cm^{-1})	$\bar{H}^{Y\omega\bar{\lambda}^Y}$
3 mm	0.485	7.9×10^4	17.6×10^8	22.7×10^8	2.4×10^{-5}	2.2×10^4	0.53
5 mm	0.488	4.1×10^4	9.7×10^8	13.7×10^8	4.8×10^{-5}	2.4×10^4	1.15
10 mm	0.497	3.8×10^4	6.6×10^8	8.7×10^8	5.2×10^{-5}	1.7×10^4	0.88
15 mm	0.491	3.6×10^4	6.1×10^8	7.4×10^8	5.5×10^{-5}	1.7×10^4	0.94

Increasing Quench Rate

intercept $\bar{\lambda}^\gamma$ used as a scale factor shows the scale of the system decreases with increasing quench rate.

The effect of quench rate on microstructure for the α - β case is shown in Figure 16. The quench rates are qualitative, based on samples taken from areas of different thickness in a poured slab. Faster quench rates give larger total surface area at a given volume fraction and thus, remembering Equation 5 for $\bar{\lambda}^\alpha$, the scale of the system decreases.

Samples were prepared in the tungsten resistance element furnace where temperatures were monitored with thermocouples. Quench rates were quantitatively determined to see the effect on the microstructure. Samples of 42 wt% ZrO_2 and 25 wt% ZrO_2 were fabricated at various quench rates, giving microstructural data about the γ - ω and the α - β cases.

For the γ - ω case, Figure 17 shows the variation of V_V^γ with quench rate. As expected, since all samples are 42 wt% ZrO_2 , the variation is small. Figure 18 shows that $S_V^{\gamma\omega}$ increases with increasing quench rate. $M_V^{\gamma\omega}$ and $|M_V^{\gamma\omega}|$ increase with increasing quench rate as seen in Figures 19 and 20. The scale factor, $\bar{\lambda}^\gamma$, decreases with increasing quench rate, Figure 21. $\bar{H}^{\gamma\omega}$ increases with increasing quench rate as shown in Figure 22. The dimensionless shape factor, $\bar{H}^{\gamma\omega}\bar{\lambda}^\gamma$, appears to be relatively constant, Figure 23. Another parameter measured for the γ - ω case was the mean colony intercept, $\bar{\lambda}^c$. This is a measure of the colony size which can be seen from Figure 24 to decrease with increasing quench rate.

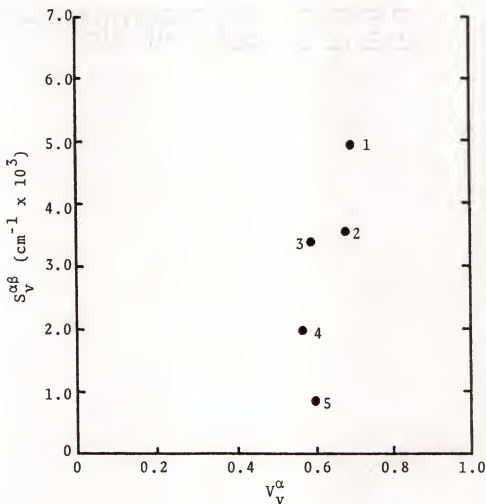


Figure 16. Effect of quench rate on volume fraction and surface area of primary alumina dendrites for fusion-cast alumina-zirconia. Points are in order of decreasing quench rate: 1 represents fastest quench rate, 5 represents slowest.

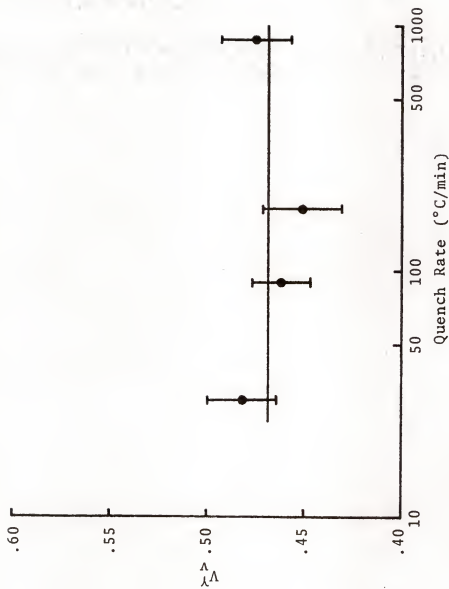


Figure 17. Volume fraction of primary zirconia in eutectic composition alumina-zirconia as a function of quench rate.

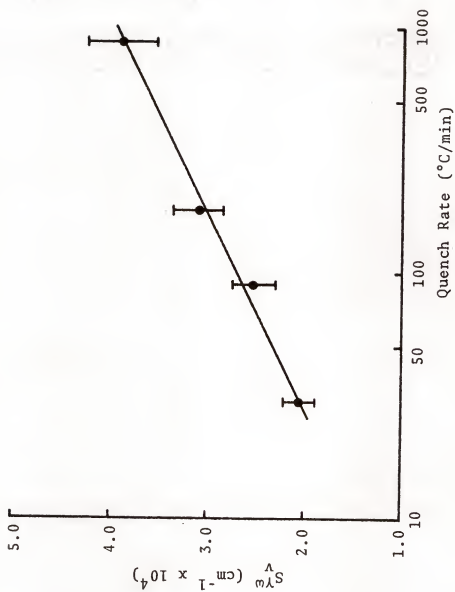


Figure 18. Total surface area of primary zirconia in eutectic composition alumina-zirconia as a function of quench rate.

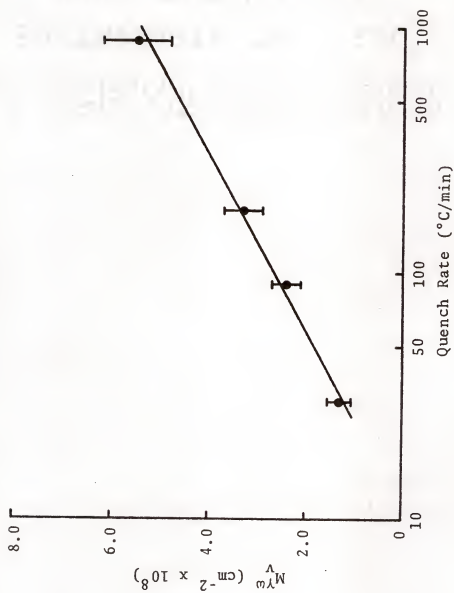


Figure 19. Total surface curvature of primary zirconia in eutectic composition alumina-zirconia as a function of quench rate.

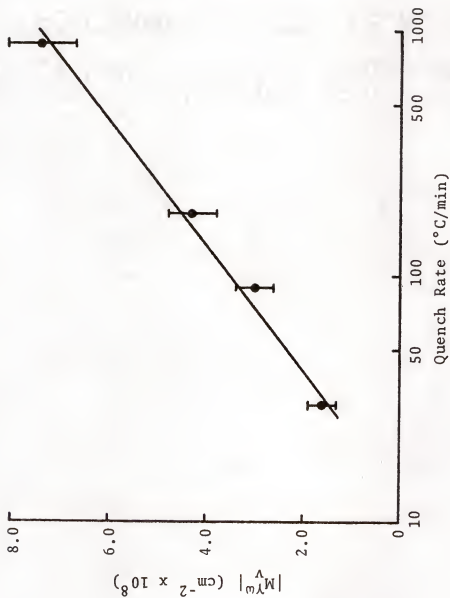


Figure 20. Absolute surface curvature of primary zirconia in eutectic composition alumina-zirconia as a function of quench rate.

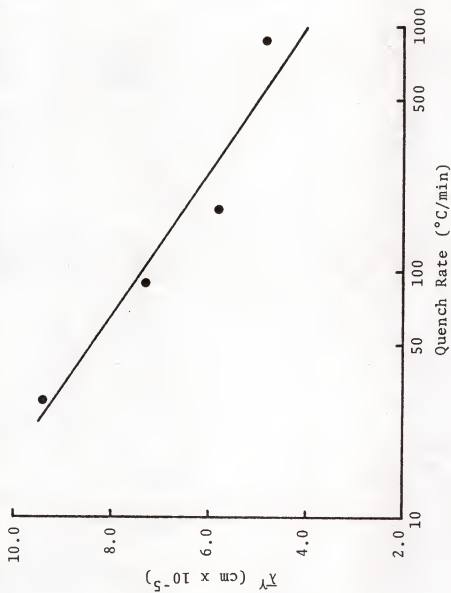


Figure 21. Mean phase intercept of primary zirconia in eutectic composition alumina-zirconia as a function of quench rate.

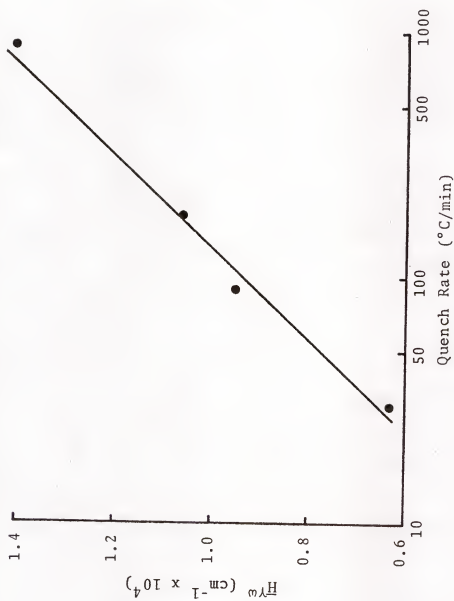


Figure 22. Average mean surface curvature of primary zirconia in eutectic composition alumina-zirconia as a function of quench rate.

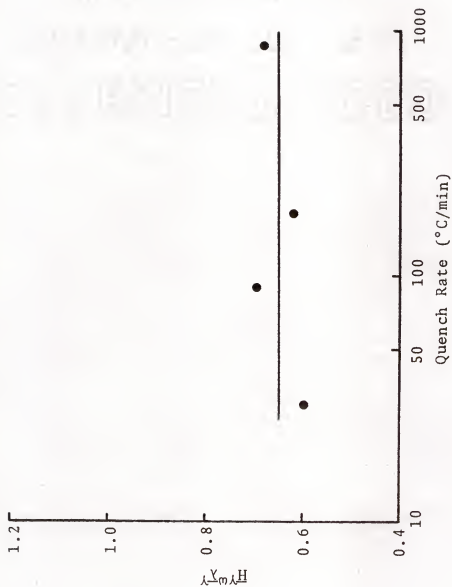


Figure 23. Shape parameter of primary zirconia in eutectic composition alumina-zirconia as a function of quench rate.

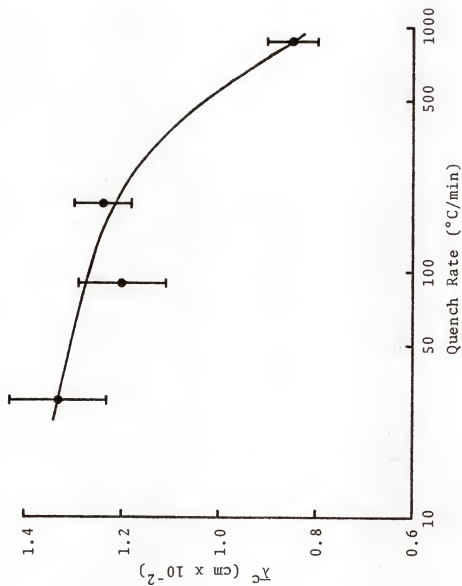


Figure 24. Mean colony intercept in eutectic composition alumina-zirconia as a function of quench rate.

For the α - β case V_V^α remains essentially constant with quench rate as would be expected since all compositions are 25 wt% ZrO_2 , see Figure 25. As shown in Figure 26, $S_V^{\alpha\beta}$ increases with increasing quench rate. Figures 27 and 28 show $M_V^{\alpha\beta}$ and $|M_V^{\alpha\beta}|$ increasing with increasing quench rate. The scale factor, $\bar{\lambda}^\alpha$, decreases with increasing quench rate, Figure 29. $\bar{H}^{\alpha\beta}$ increases as can be seen from Figure 30. The shape factor, $\bar{H}^{\alpha\beta}\bar{\lambda}^\alpha$, may increase with increasing quench rate as can be seen in Figure 31, although later data show that this conclusion is probably based on fortuitous scatter in data values.

The effect of impurities on the microstructure was investigated. Impurities are always present to some degree, so the range of impurity concentrations studied was that which might be found in commercial quality raw materials. The impurities studied were also studied at increasing concentrations up to concentrations which produced a significant amount of a third phase. Impurities studied in detail were CaO , TiO_2 , Cr_2O_3 and V_2O_5 . CaO was picked to see the effect of stabilizing the zirconia in the cubic modification and TiO_2 , Cr_2O_3 and V_2O_5 are known to strengthen alumina.

Table II shows the effect of CaO and TiO_2 on some experimental commercial samples of the eutectic composition nominally. For a given quench rate, 5 wt% TiO_2 decreased $S_V^{\gamma\omega}$, $M_V^{\gamma\omega}$ and $\bar{H}^{\gamma\omega}$ while increasing the scale of the microstructure, $\bar{\lambda}^\gamma$. At a given quench rate, 3 wt% $CaCO_3$ showed the same general trends. Different casting methods were used for each

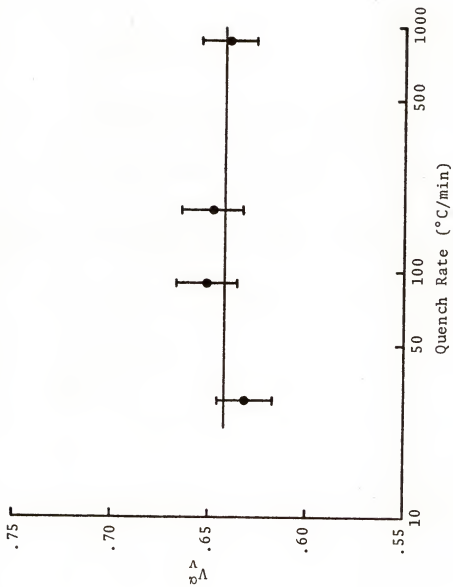


Figure 25. Volume fraction of primary alumina dendrites in 25 wt% ZrO_2 -75 wt% Al_2O_3 as a function of quench rate.

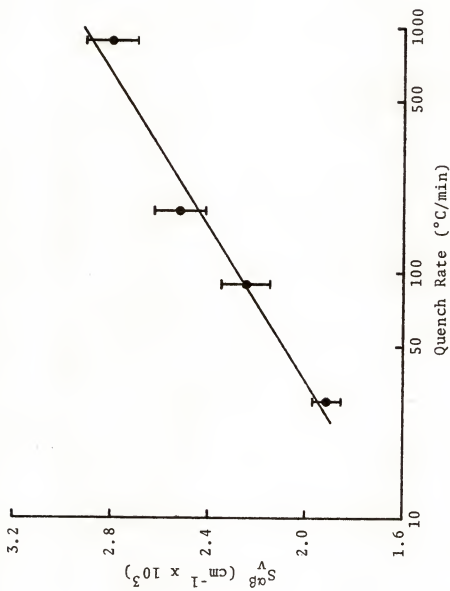


Figure 26. Total surface area of primary alumina dendrites in 25 wt% ZrO_2 -75 wt% Al_2O_3 as a function of quench rate.

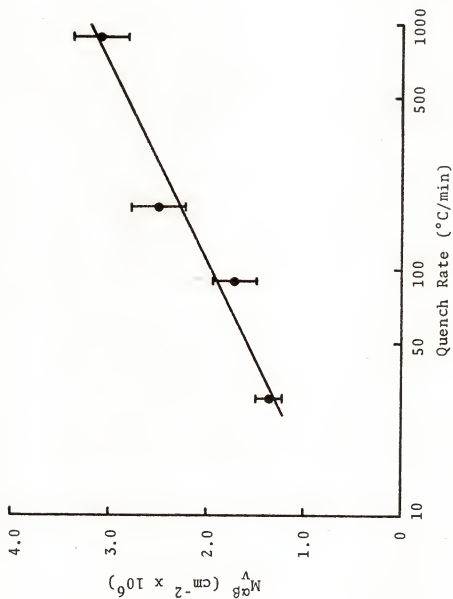


Figure 27. Total surface curvature of primary alumina dendrites in 25 wt% ZrO_2 -75 wt% Al_2O_3 as a function of quench rate.

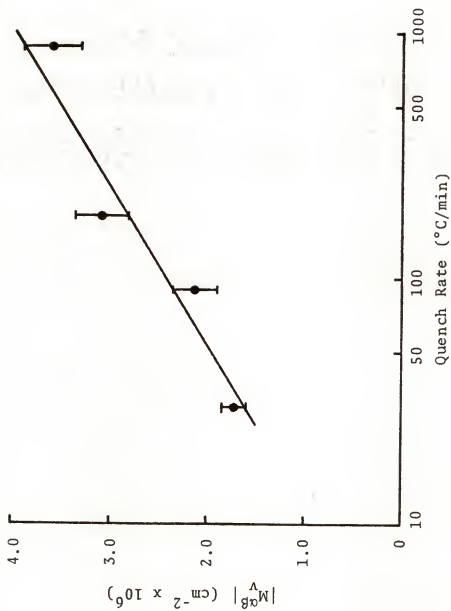


Figure 28. Absolute surface curvature of primary alumina dendrites in 25 wt% ZrO_2 -75 wt% Al_2O_3 as a function of quench rate.

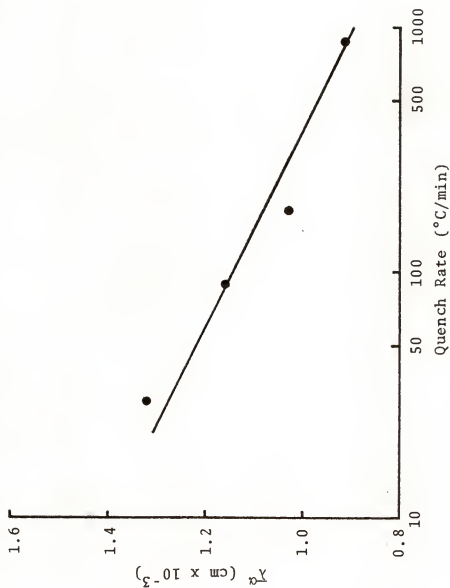


Figure 29. Mean phase intercept of primary alumina dendrites in 25 wt% ZrO_2 -75 wt% Al_2O_3 as a function of quench rate.

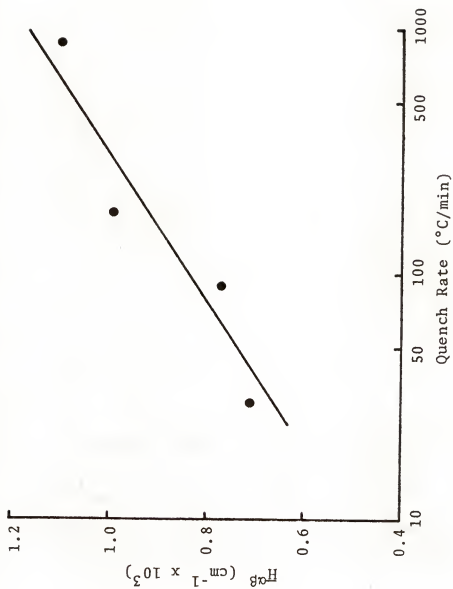


Figure 30. Average mean surface curvature of primary alumina dendrites in 25 wt% ZrO_2 -75 wt% Al_2O_3 as a function of quench rate.

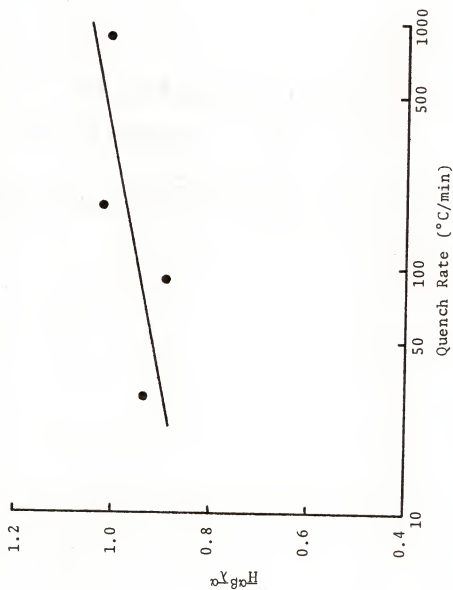


Figure 31. Shape parameter of primary alumina dendrites in 25 wt% ZrO_2 -75 wt% Al_2O_3 as a function of quench rate.

Table II

Chemical Control of Microstructure

Wt% TiO ₂		V_V^Y	$S_V^{Y\omega}$ (cm ⁻¹)	$M_V^{Y\omega}$ (cm ⁻²)	$ M_V^{Y\omega} $ (cm ⁻²)	$\bar{\lambda}^Y$ (cm)	$\bar{H}^{Y\omega}$ (cm ⁻¹)	$\bar{H}^{Y\omega}\bar{\lambda}^Y$
0		0.46	4.8×10^4	6.1×10^8	7.8×10^8	3.8×10^{-5}	12.7×10^3	0.47
5		0.44	3.5×10^4	3.2×10^8	6.2×10^8	5.0×10^{-5}	9.1×10^3	0.455

Wt% CaCO ₃		V_V^Y	$S_V^{Y\omega}$ (cm ⁻¹)	$M_V^{Y\omega}$ (cm ⁻²)	$ M_V^{Y\omega} $ (cm ⁻²)	$\bar{\lambda}^Y$ (cm)	$\bar{H}^{Y\omega}$ (cm ⁻¹)	$\bar{H}^{Y\omega}\bar{\lambda}^Y$
Faster Quench Rate	0	0.40	1.7×10^4	1.3×10^8	1.7×10^8	9.4×10^{-5}	7.6×10^3	0.71
	3	0.39	1.3×10^4	0.74×10^8	1.1×10^8	12.0×10^{-5}	5.7×10^3	0.68
Slower Quench Rate	0	0.37	1.4×10^4	2.0×10^8	2.2×10^8	10.6×10^{-5}	14.3×10^3	1.52
	3	0.35	1.2×10^4	0.89×10^8	0.97×10^8	11.7×10^{-5}	7.4×10^3	0.87

set of data in Table II, accounting for the difference in the 0 wt% values.

Results of samples of the eutectic composition with third components added and fired in the tungsten resistance element furnace are shown in Figures 32 through 39. The quench rate for all samples was approximately 880°C/min. The additives appear to have a negligible effect on V_V^Y excepting CaO. Additions of CaO and TiO_2 decrease $S_V^{Y\omega}$ while Cr_2O_3 and V_2O_5 have a small effect in comparison. The changes in $M_V^{Y\omega}$ and $|M_V^{Y\omega}|$ are the same, CaO and TiO_2 decrease them and Cr_2O_3 and V_2O_5 have no measurable effect. The scale factor, $\bar{\lambda}^Y$, remains relatively constant for Cr_2O_3 and V_2O_5 but increases for CaO and TiO_2 . $\bar{H}^{Y\omega}$ decreases for CaO and TiO_2 but changes little for Cr_2O_3 and V_2O_5 allowing for some scatter. The shape parameter, $\bar{H}^{Y\omega}\bar{\lambda}^Y$, remains relatively constant with a slight increase in value possible for all additives. $\bar{\lambda}^C$ increases for CaO and Cr_2O_3 (after an initial decrease) and decreases for TiO_2 and V_2O_5 .

The effects of CaO, TiO_2 , Cr_2O_3 and V_2O_5 on the microstructure of 25 wt% ZrO_2 cast materials are shown in Figures 40 through 46. V_V^α increases slightly with the third component additions. $S_V^{\alpha\beta}$ decreases in all cases. $M_V^{\alpha\beta}$ and $|M_V^{\alpha\beta}|$ decrease in all cases also. The scale factor, $\bar{\lambda}^\alpha$, increases with all the additions. $\bar{H}^{\alpha\beta}$ decreases especially in the V_2O_5 case. The shape parameter remains fairly constant for TiO_2 and V_2O_5 but decreases for CaO and Cr_2O_3 .

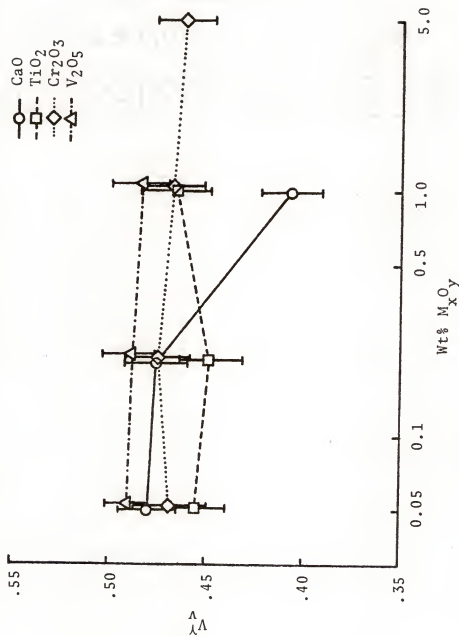


Figure 32. Effect of impurities on volume fraction of primary zirconia in eutectic composition alumina-zirconia. Quench rate is 880°C/min.

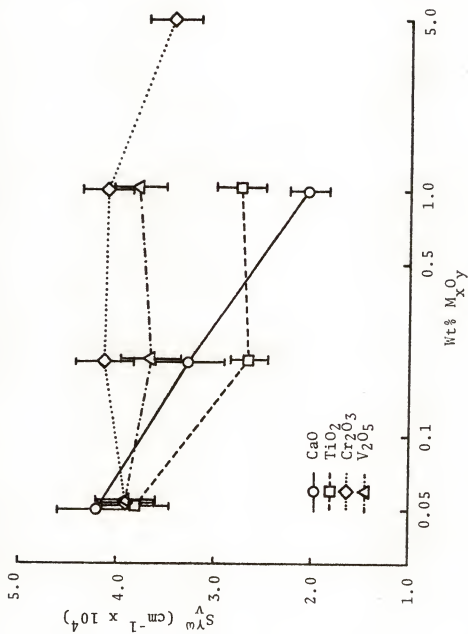


Figure 33. Effect of impurities on total surface area of primary zirconia in eutectic composition alumina-zirconia. Quench rate is 880°C/min.

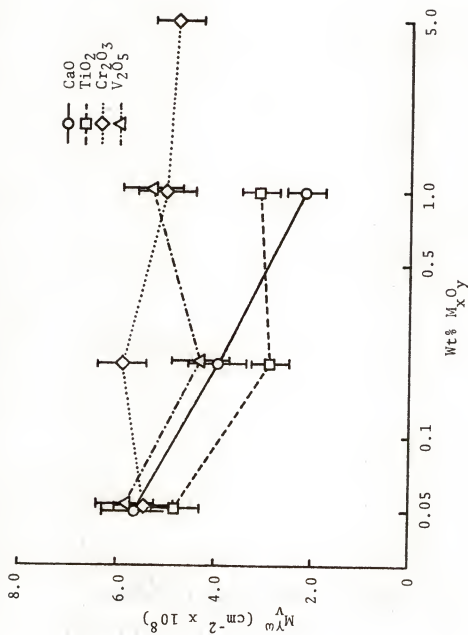


Figure 34. Effect of impurities on total surface curvature of primary zirconia in eutectic composition alumina-zirconia. Quench rate is $880^\circ\text{C}/\text{min}$.

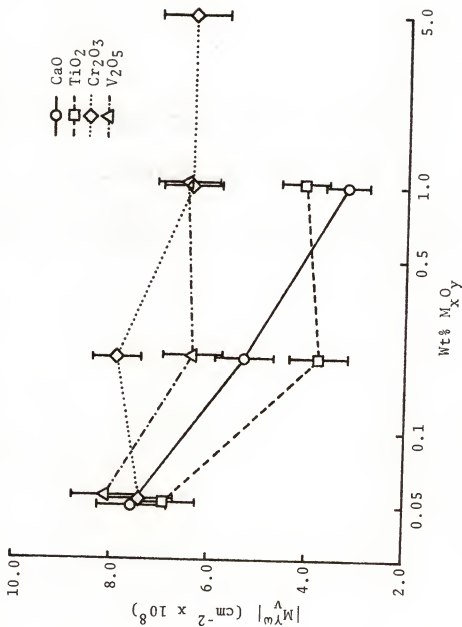


Figure 35. Effect of impurities on absolute surface curvature of primary zirconia in eutectic composition alumina-zirconia. Quench rate is 880°C/min.

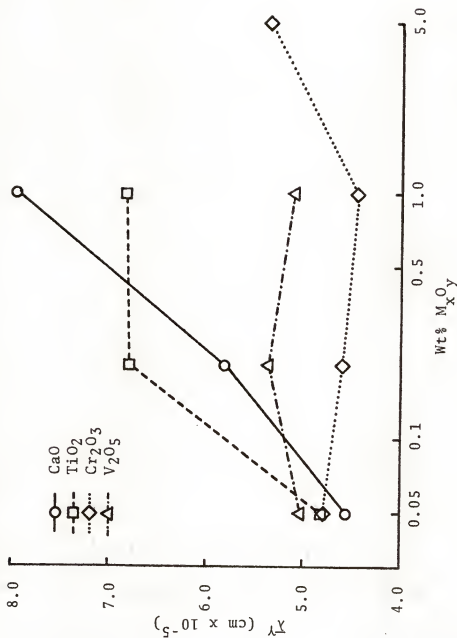


Figure 36. Effect of impurities on mean phase intercept of primary zirconia in eutectic composition alumina-zirconia. Quench rate is 880°C/min.

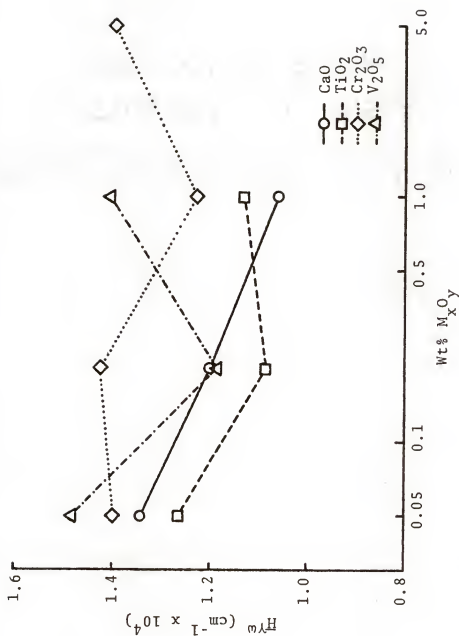


Figure 37. Effect of impurities on average mean surface curvature of primary zirconia in eutectic composition alumina-zirconia. Quench rate is 880°C/min.

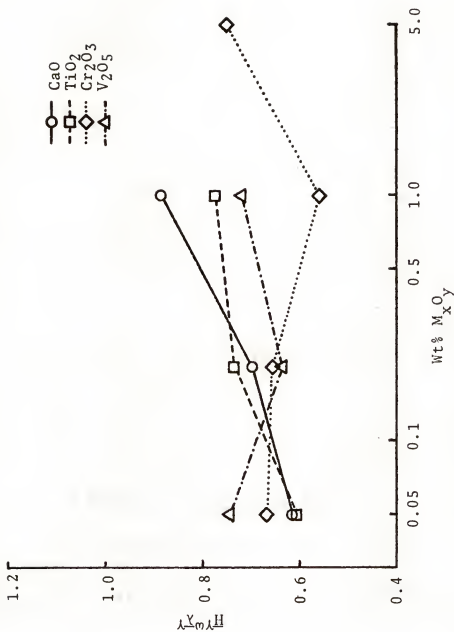


Figure 38. Effect of impurities on shape parameter of primary zirconia in eutectic composition alumina-zirconia. Quench rate is 880°C/min.

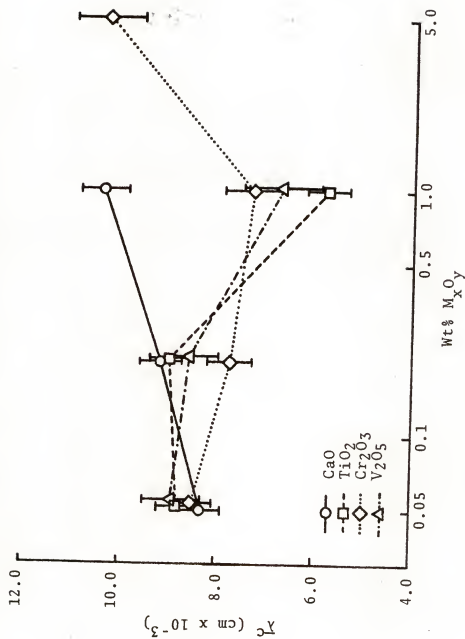


Figure 39. Effect of impurities on mean colony intercept in eutectic composition alumina-zirconia. Quench rate is 880°C/min.

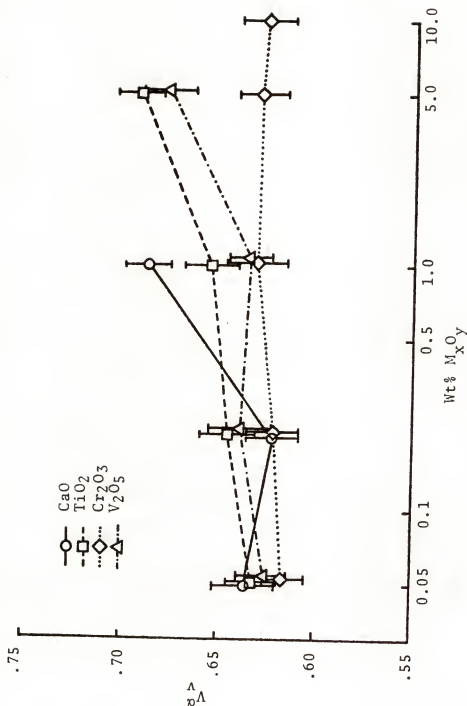


Figure 40. Effect of impurities on volume fraction of primary alumina dendrites in 25 wt% ZrO_2 -75 wt% Al_2O_3 . Quench rate is 880°C/min.

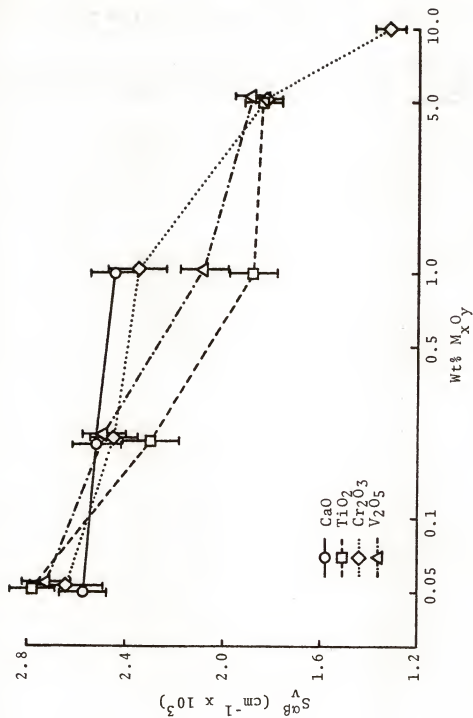


Figure 41. Effect of impurities on total surface area of primary alumina dendrites in 25 wt% ZrO_2 -75 wt% Al_2O_3 . Quench rate is $880^\circ C/min$.

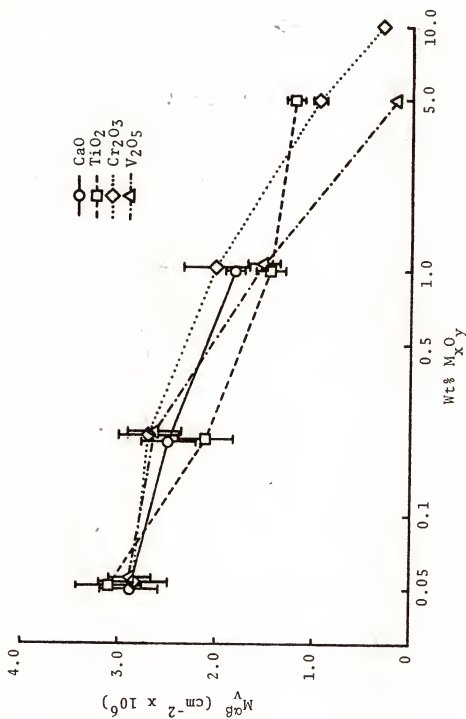


Figure 42. Effect of impurities on total surface curvature of primary alumina dendrites in 25 wt% ZrO₂-75 wt% Al₂O₃. Quench rate is 880°C/min.

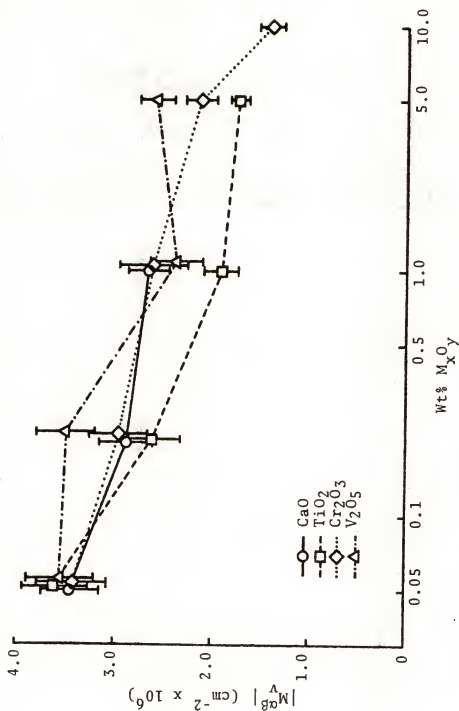


Figure 43. Effect of impurities on absolute surface curvature of primary alumina dendrites in 25 wt% ZrO₂-75 wt% Al₂O₃. Quench rate is 880°C/min.

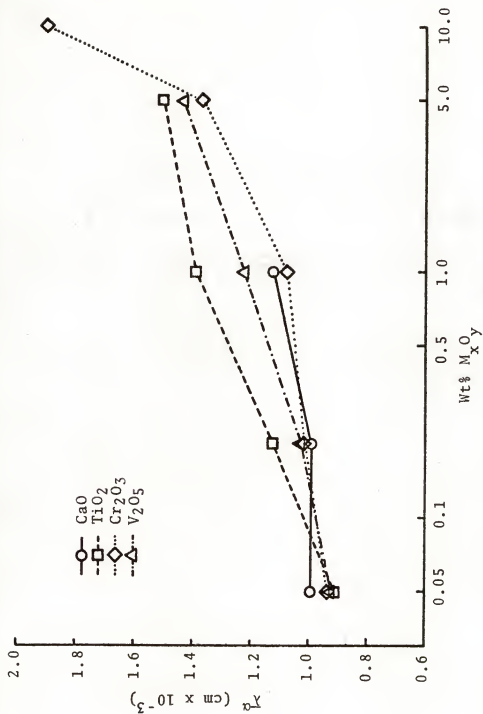


Figure 44. Effect of impurities on mean phase intercept of primary alumina dendrites in 25 wt% ZrO₂-75 wt% Al₂O₃. Quench rate is 880°C/min.

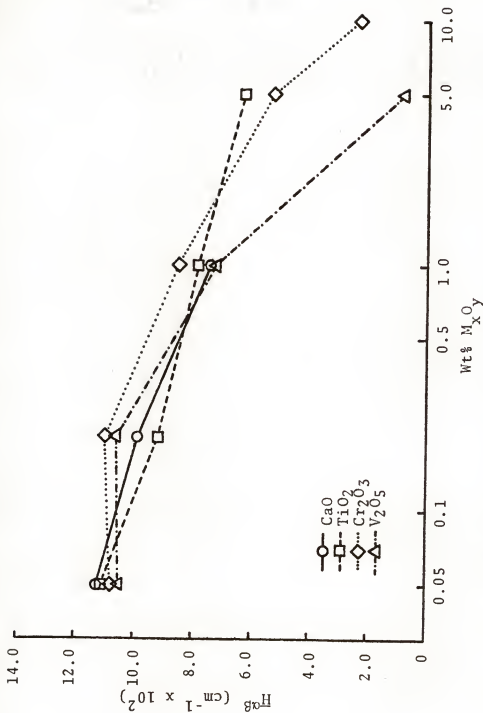


Figure 45. Effect of impurities on average mean surface curvature of primary alumina dendrites in 25 wt% ZrO_2 -75 wt% Al_2O_3 . Quench rate is $880^\circ\text{C}/\text{min}$.

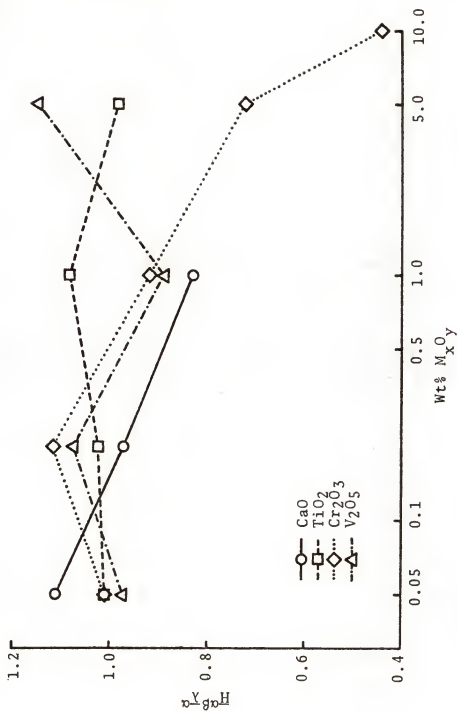


Figure 46. Effect of impurities on shape parameter of primary alumina dendrites in 25 wt% ZrO_2 -75 wt% Al_2O_3 . Quench rate is 880°C/min.

Friability

Three different tests were used to measure friability. Not every sample was tested by all three tests but enough cross-checking between tests with the same sample was done to see if the three tests do indeed measure the same mechanical property called friability. Figure 47 shows the correlation between the DeBeers Friatester results and the ball mill test. A nearly linear relation exists with a slight deviation at high friabilities. A linear correlation exists between the ball mill test and the microfriability test as can be seen from Figure 48. A nearly linear relation was found between the DeBeers test and the microfriability test, Figure 49. These data show that the three tests measure the same mechanical property. The major difference between them is the amount of material required to make the test: about 100 gms for the ball mill test, about 1 gm for the microfriability test and on the order of tenths of a gram for the DeBeers test.

Microstructural Control of Friability

The dependence of friability on microstructure can be seen from the following data. Samples are experimental commercial materials prepared by a variety of casting techniques. Microstructural data are plotted with friability and toughness. The friability scale on the graphs is reversed from the normal convention for ease in comparing results. All samples are of nearly the eutectic composition being 42 to 45 wt% ZrO_2 . V_v^Y is essentially constant so no correlation was found

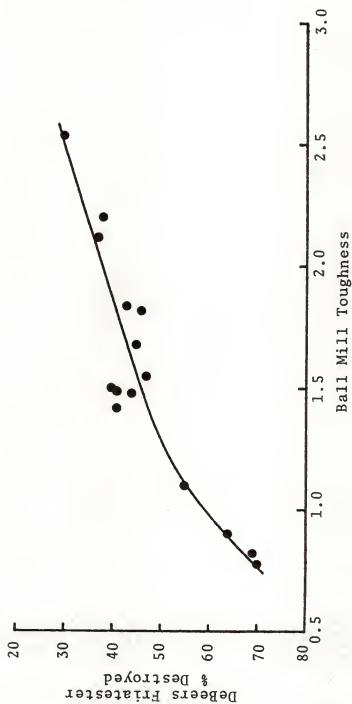


Figure 47. Correlation between DeBeers Friability and ball mill toughness.

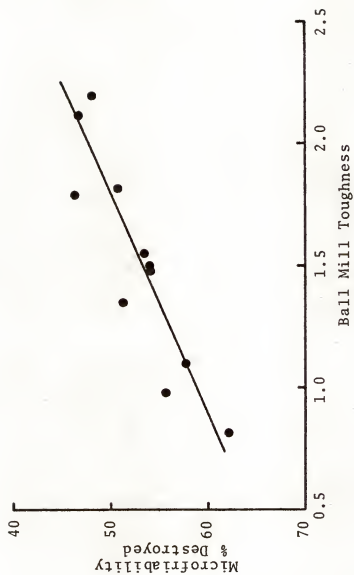


Figure 48. Correlation between microfriability and ball mill toughness.

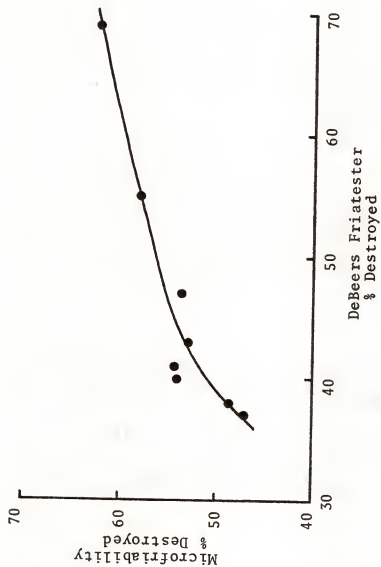


Figure 49. Correlation between microfriability and DeBeers Friability.

with friability. Figure 50 shows the dependence of friability (or toughness) on $S_V^{\gamma\omega}$. As $S_V^{\gamma\omega}$ increases, the friability decreases and a tougher material is obtained. As $M_V^{\gamma\omega}$ and $|M_V^{\gamma\omega}|$ increase, the friability decreases as shown in Figures 51 and 52. Increasing the scale of the microstructure yields a more friable material as seen in Figure 53. As $\bar{H}^{\gamma\omega}$ increases the friability increases, although this correlation is not as good as some of the others as seen from the scatter in the data in Figure 54. The shape factor, $\bar{H}^{\gamma\omega}\bar{\lambda}^{\gamma}$, appears to increase the friability as it increases, but due to the scatter in the data this may not be a viable conclusion as seen in Figure 55.

Samples prepared in the tungsten resistance element furnace of composition 42 wt% ZrO_2 show essentially the same results as the preceding series. The only real difference is the shape factor, $\bar{H}^{\gamma\omega}\bar{\lambda}^{\gamma}$, appears to have no effect on friability in this series. Figures 56 through 61 show the dependence of microfriability on microstructure.

A 25 wt% ZrO_2 compositional series was also prepared in the tungsten resistance element furnace. Microstructural data from these samples are plotted against microfriability in Figures 62 through 67. As $S_V^{\alpha\beta}$, $M_V^{\alpha\beta}$ and $|M_V^{\alpha\beta}|$ increase, the friability decreases. Friability increases with increasing $\bar{\lambda}^{\alpha}$, the scale factor. As $\bar{H}^{\alpha\beta}$ increases friability decreases. The shape factor, $\bar{H}^{\alpha\beta}\bar{\lambda}^{\alpha}$, changes slightly with a decrease causing an increase in friability.

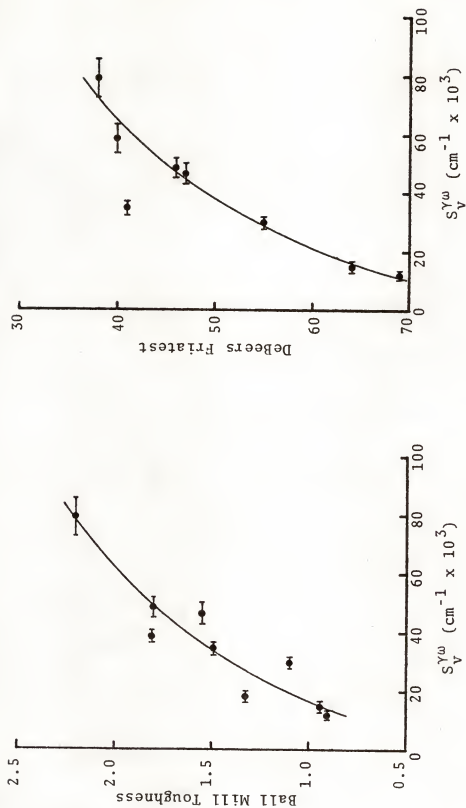


Figure 50. Dependence of toughness and friability on total surface area of primary zirconia in eutectic composition alumina-zirconia.

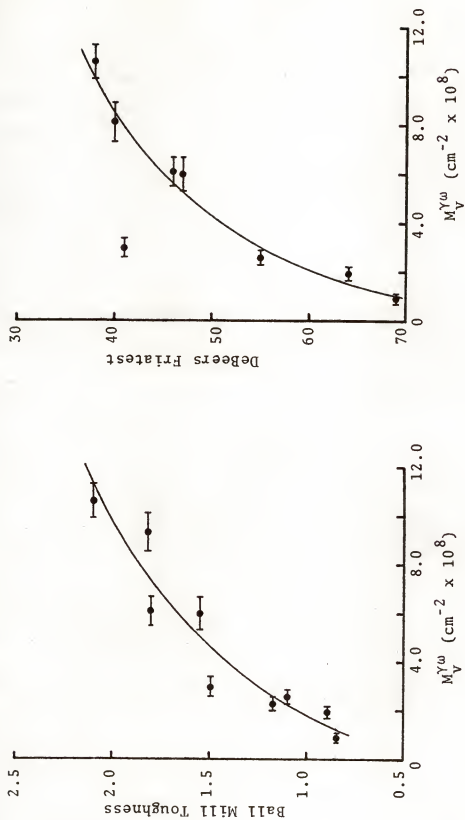


Figure 51. Dependence of toughness and friability on total surface curvature of primary zirconia in eutectic composition alumina-zirconia.

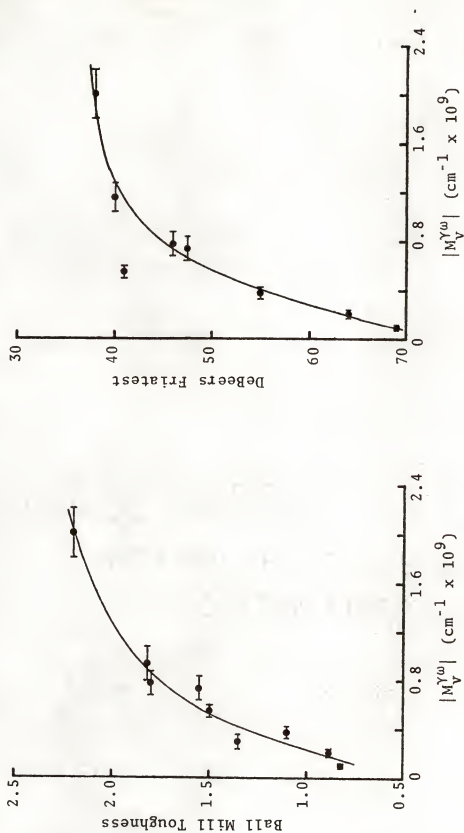


Figure 52. Dependence of toughness and friability on absolute surface curvature of primary zirconia in eutectic composition alumina-zirconia.

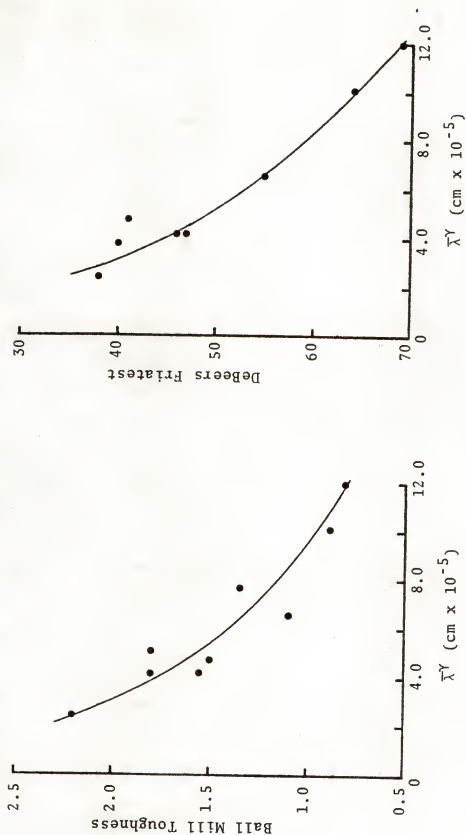


Figure 53. Dependence of toughness and friability on mean phase intercept of primary zirconia in eutectic composition alumina-zirconia.

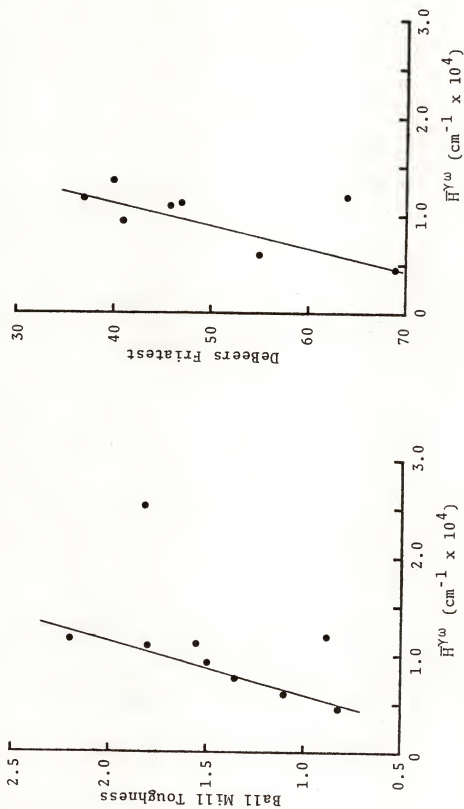


Figure 54. Dependence of toughness and friability on average mean surface curvature of primary zirconia in eutectic composition alumina-zirconia.

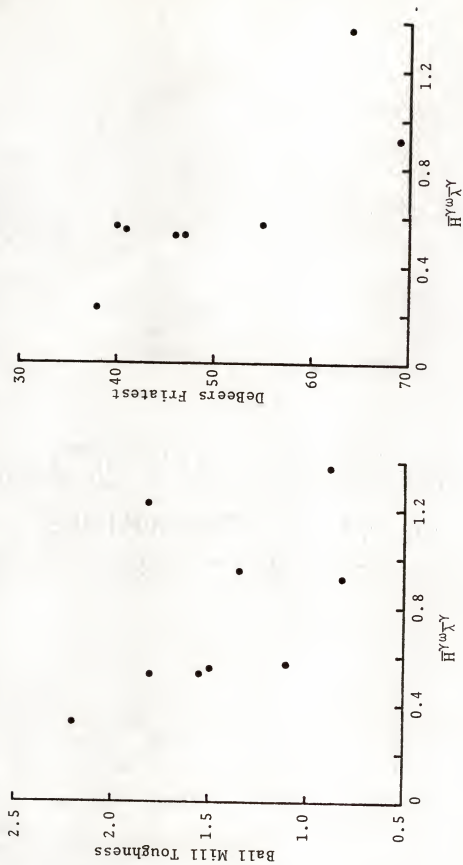


Figure 55. Dependence of toughness and friability on shape parameter of primary zirconia in eutectic composition alumina-zirconia.

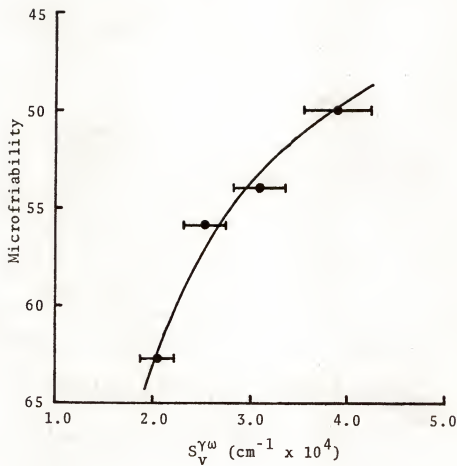


Figure 56. Dependence of microfriability on total surface area of primary zirconia in eutectic composition alumina-zirconia.

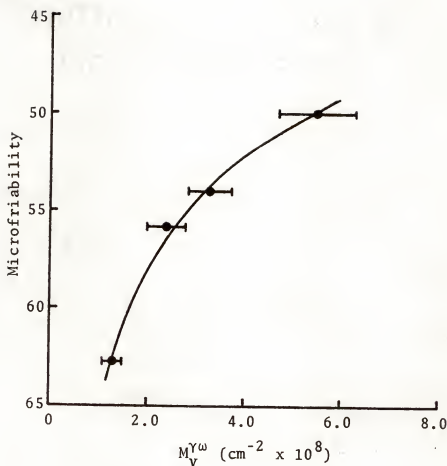


Figure 57. Dependence of microfriability on total surface curvature of primary zirconia in eutectic composition alumina-zirconia.

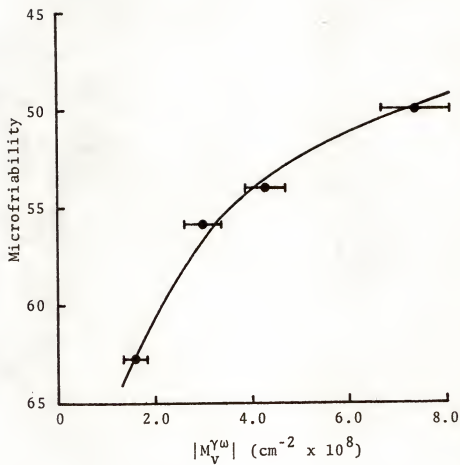


Figure 58. Dependence of microfriability on absolute surface curvature of primary zirconia in eutectic composition alumina-zirconia.

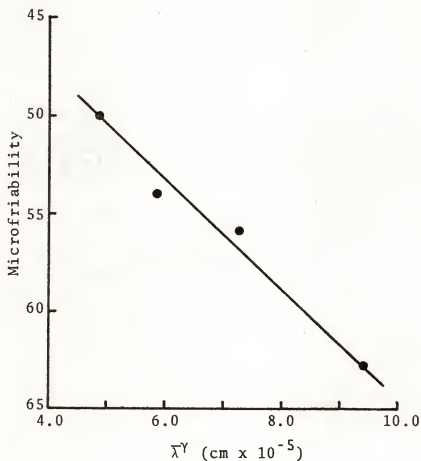


Figure 59. Dependence of microfriability on mean phase intercept of primary zirconia in eutectic composition alumina-zirconia.

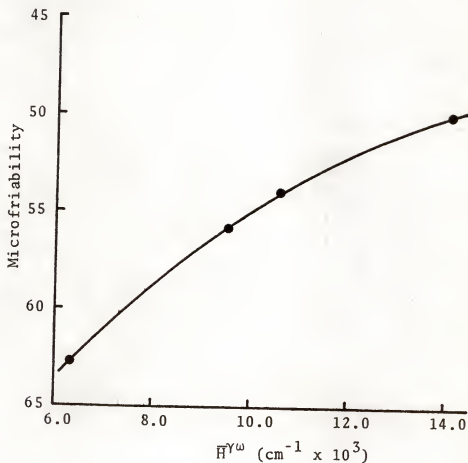


Figure 60. Dependence of microfriability on average mean surface curvature of primary zirconia in eutectic composition alumina-zirconia.

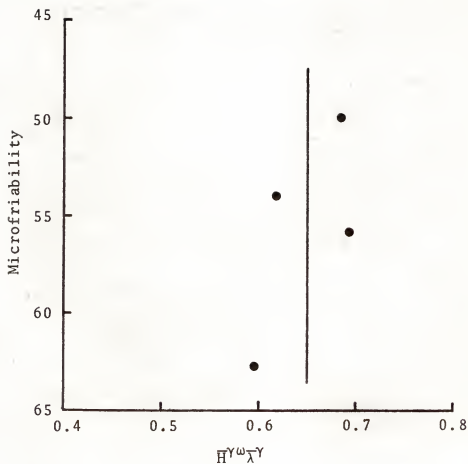


Figure 61. Dependence of microfriability on shape parameter of primary zirconia in eutectic composition alumina-zirconia.

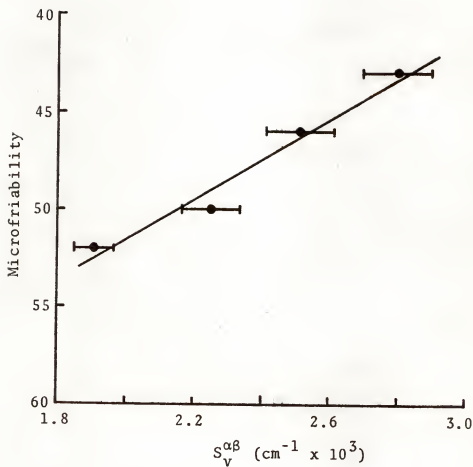


Figure 62. Dependence of microfriability on total surface area of primary alumina dendrites in 25 wt% ZrO_2 -75 wt% Al_2O_3 .

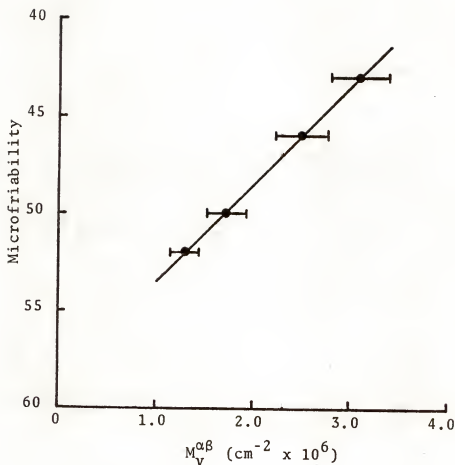


Figure 63. Dependence of microfibrability on total surface curvature of primary alumina dendrites in 25 wt% ZrO_2 -75 wt% Al_2O_3 .

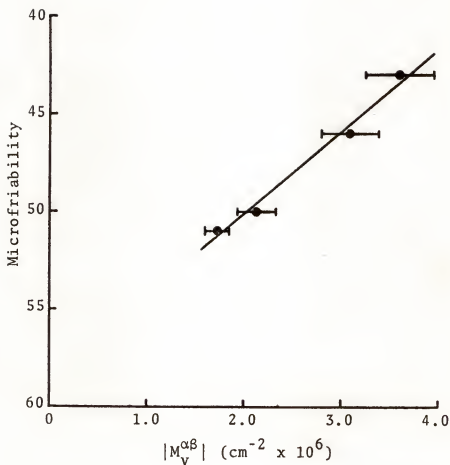


Figure 64. Dependence of microfriability on absolute surface curvature of primary alumina dendrites in 25 wt% ZrO_2 -75 wt% Al_2O_3 .

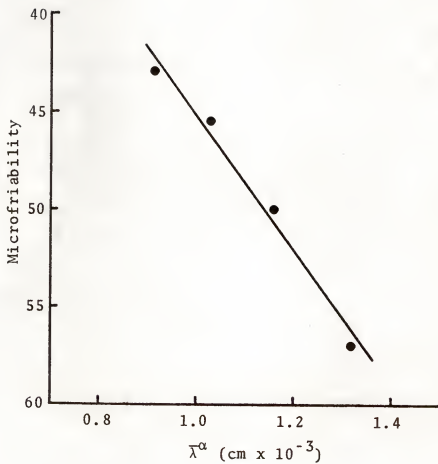


Figure 65. Dependence of microfriability on mean phase intercept of primary alumina dendrites in 25 wt% ZrO_2 -75 wt% Al_2O_3 .

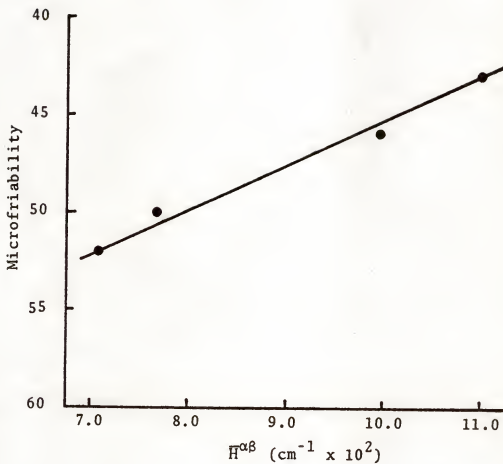


Figure 66. Dependence of microfibrability on average mean surface curvature of primary alumina dendrites in 25 wt% ZrO_2 -75 wt% Al_2O_3 .

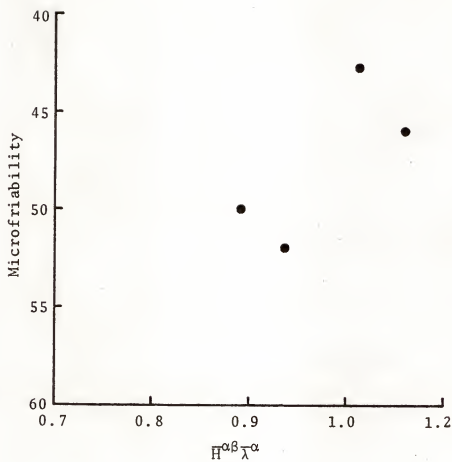


Figure 67. Dependence of microfriability on shape parameter of primary alumina dendrites in 25 wt% ZrO_2 -75 wt% Al_2O_3 .

One of the objectives of this study was to control the friability of the alumina-zirconia material by controlling the processing variables. This could have been done by going through a matrix of processing controls and picking the process that gave the best results as defined by the problem. This would perhaps yield a suitable material for most problems but may give only speculative information on why one process worked better than others. By analyzing how microstructure controls friability and then how to control the microstructure, it can be seen why and how certain processing variations affect the friability. Figure 68 shows the control quench rate has on the friability. The preceding figures help explain how the quench rate actually controls the friability.

Impurity Control of Friability

Impurities have been shown to control the microstructure to a certain extent. Microstructure has been shown to control the friability. Therefore impurities should control the friability. This turns out to be true, but in some cases impurities control the friability to an extent beyond that expected from the microstructural changes induced by the impurities. This illustrates the fact that the friability is not controlled by microstructure alone but depends on many things. No one basic property has even been shown to control friability exclusively.

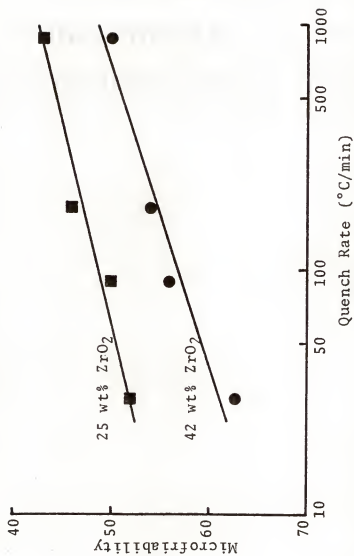


Figure 68. Dependence of microfriability on quench rate for 25 wt% ZrO₂-75 wt% Al₂O₃ and 42 wt% ZrO₂-58 wt% Al₂O₃.

The microstructure does control friability to a large extent, though, and probably the next most important factor is the amount and type of impurities or alloying additions. Porosity is an important aspect of the microstructure which controls friability and will be discussed later.

For the eutectic composition, γ - ω case, the effects of the additions of CaO , TiO_2 , Cr_2O_3 and V_2O_5 on the friability can be seen from Figures 69 through 74. For reference, the microstructural effects alone are shown also. CaO essentially affects the friability by its microstructural effects. TiO_2 , V_2O_5 and Cr_2O_3 give a tougher material than the microstructural characterizations predict.

The 25 wt% ZrO_2 case gives slightly different results as shown in Figures 75 through 80. The V_2O_5 produces the changes in friability expected from the microstructural changes. TiO_2 gives the expected change in friability except at large wt% TiO_2 values a significantly weaker grain is produced. CaO gives a more friable material than predicted, while Cr_2O_3 gives a substantial decrease in friability over that predicted by the microstructure.

Data reported above were for additions below which a third phase appeared on the microstructural sections used in the counting measurements. Appearance of a third phase resulted in very large increases in the friabilities of the CaO materials as seen in Figures 81 and 82. Third-phase additions in the TiO_2 materials produced a weaker grain in the γ - ω case and nearly the same effect as CaO in the α - β

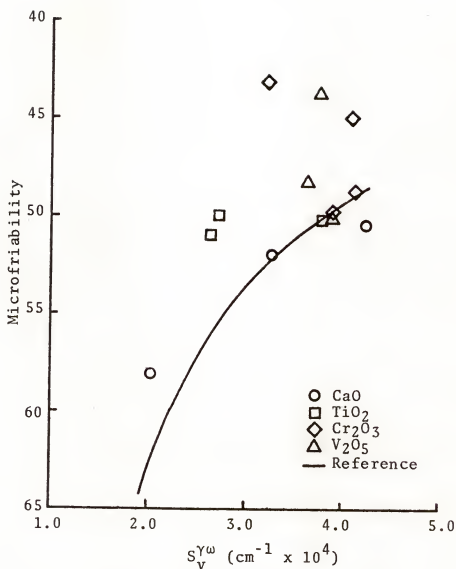


Figure 69. Effects of impurities on microfriability beyond the dependence on total surface area of primary zirconia in eutectic composition alumina-zirconia.

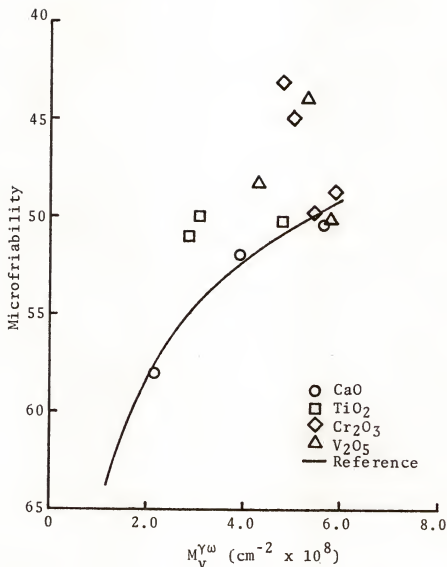


Figure 70. Effects of impurities on microfriability beyond the dependence on total surface curvature of primary zirconia in eutectic composition alumina-zirconia.

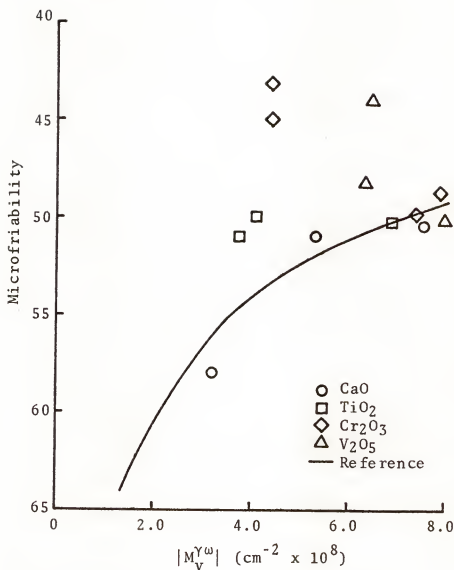


Figure 71. Effects of impurities on microfriability beyond the dependence on absolute surface curvature of primary zirconia in eutectic composition alumina-zirconia.

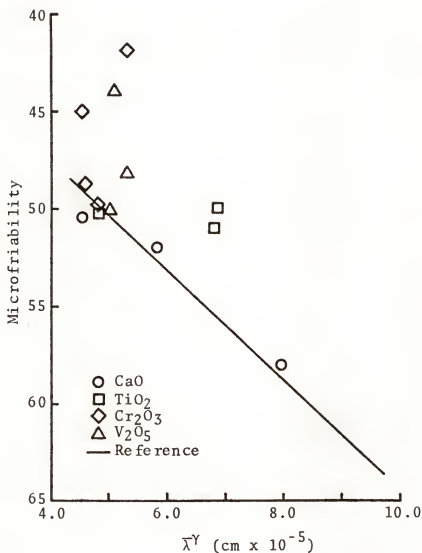


Figure 72. Effects of impurities on microfriability beyond the dependence on mean phase intercept of primary zirconia in eutectic composition alumina-zirconia.

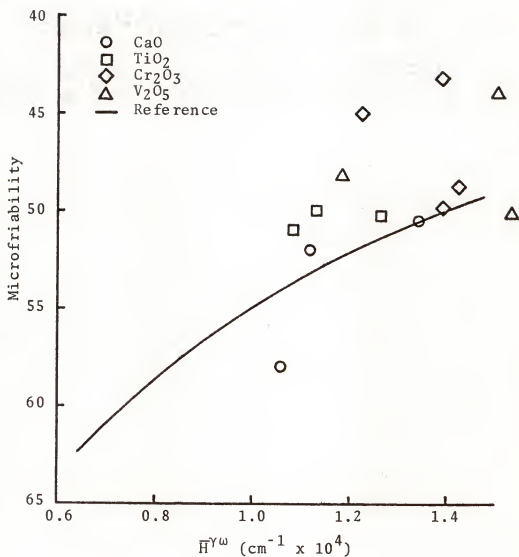


Figure 73. Effects of impurities on microfriability beyond the dependence on average mean surface curvature of primary zirconia in eutectic composition alumina-zirconia.

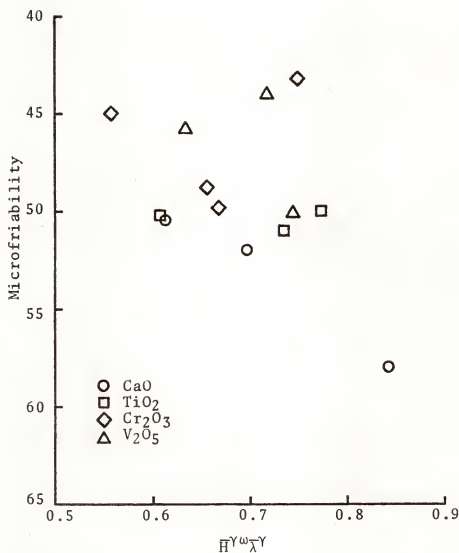


Figure 74. Effects of impurities on microfriability beyond the dependence on shape parameter of primary zirconia in eutectic composition alumina-zirconia.

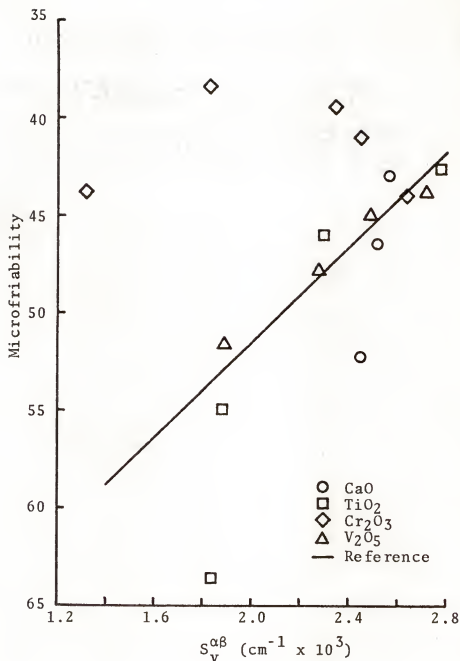
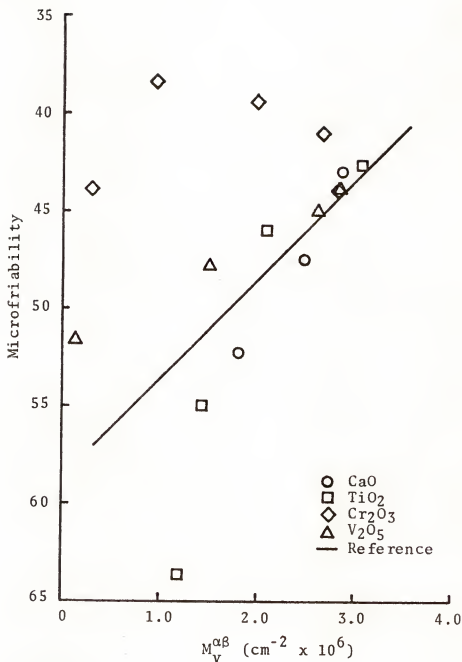


Figure 75. Effects of impurities on microfriability beyond the dependence on total surface area of primary alumina dendrites in 25 wt% ZrO₂-75 wt% Al₂O₃.



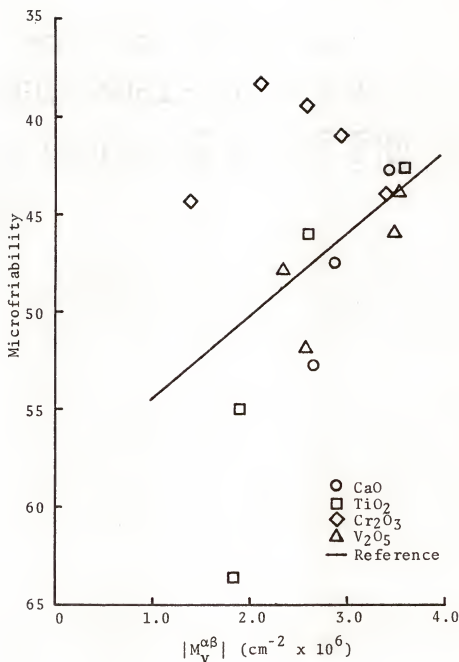


Figure 77. Effects of impurities on microfriability beyond the dependence on absolute surface curvature of primary alumina dendrites in 25 wt% ZrO₂-75 wt% Al₂O₃.

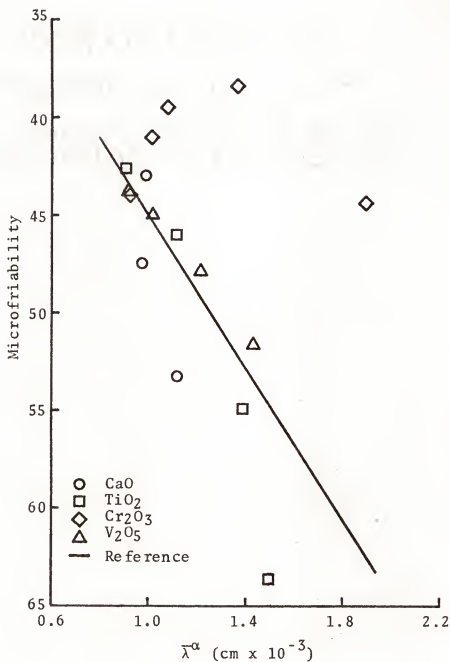


Figure 78: Effects of impurities on microfriability beyond the dependence on mean phase intercept of primary alumina dendrites in 25 wt% ZrO₂-75 wt% Al₂O₃.

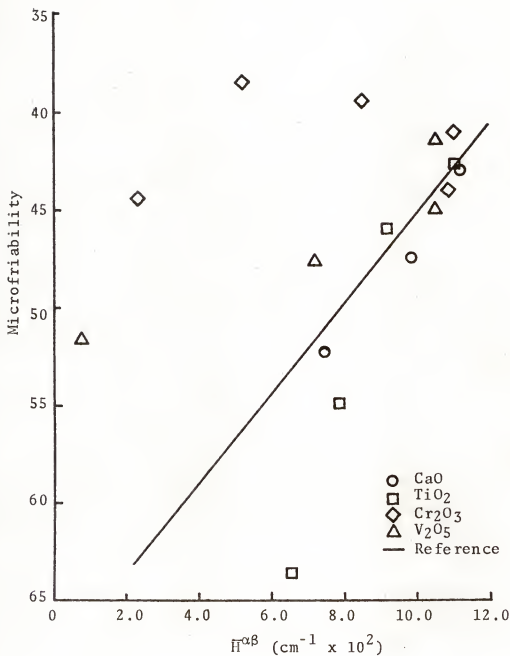


Figure 79. Effects of impurities on microfriability beyond the dependence on average mean surface curvature of primary alumina dendrites in 25 wt% ZrO₂-75 wt% Al₂O₃.

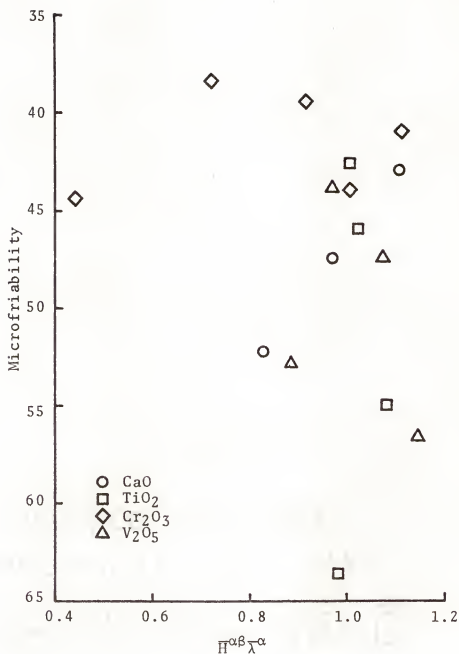


Figure 80. Effects of impurities on microfriability beyond the dependence on shape parameter of primary alumina dendrites in 25 wt% ZrO₂-75 wt% Al₂O₃.

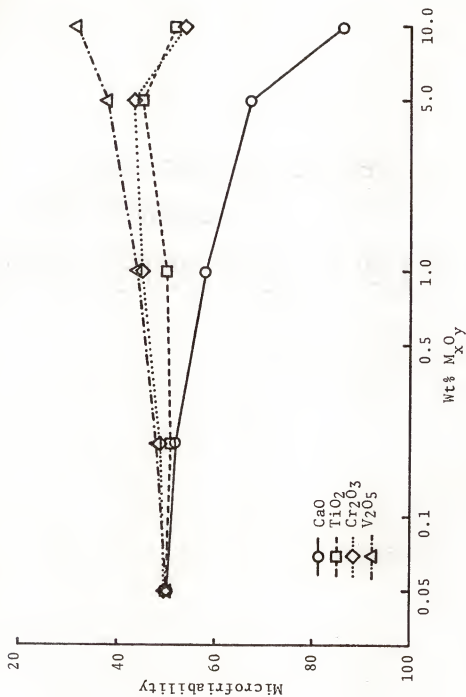


Figure 81. Dependence of microfriability on impurities for eutectic composition alumina-zirconia. Quench rate is 880°C/min.

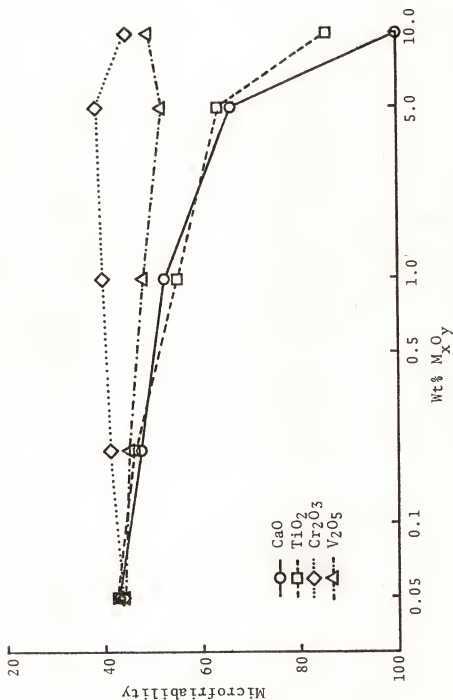


Figure 82. Dependence of microfriability on impurities for 25 wt% ZrO_2 -75 wt% Al_2O_3 . Quench rate is 880°C/min.

case. The V_2O_5 produced a stronger grain in the γ - ω case on the third-phase addition and a slightly weaker grain in the α - β case. A third phase was not observed on additions of Cr_2O_3 and was not expected since alumina and chromia are isomorphous compounds. Figures 81 and 82 are of practical importance in showing the effect of alloying additions on the friability of alumina-zirconia but do not contain the information of previous plots necessary to explore mechanisms of toughening.

Density

The density of a material gives a measure of the porosity if the true density is known. Porosity has been shown to influence mechanical properties of many materials. Porosity affects the friability of the alumina-zirconia material also. Figures 83 and 84 show how the porosity affects the friability. Figure 83 is for samples prepared in the tungsten resistance element furnace and Figure 84 is for the experimental commercial materials. In general, the data show that a low density material is very friable whereas the higher density materials have lower friability. High density does not insure low friability but low density insures high friability. Figure 85 shows a similar correlation for 25 wt% ZrO_2 materials. A theoretical density is marked on the preceding plots and was calculated assuming no solid solution in either the alumina or the zirconia.

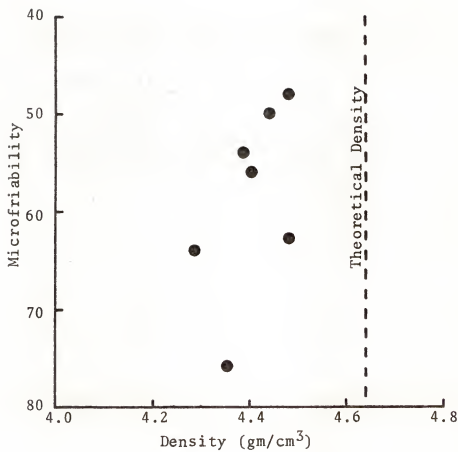


Figure 83. Microfriability as a function of density for 42 wt% ZrO₂-58 wt% Al₂O₃. Theoretical density assumes no solid solution.

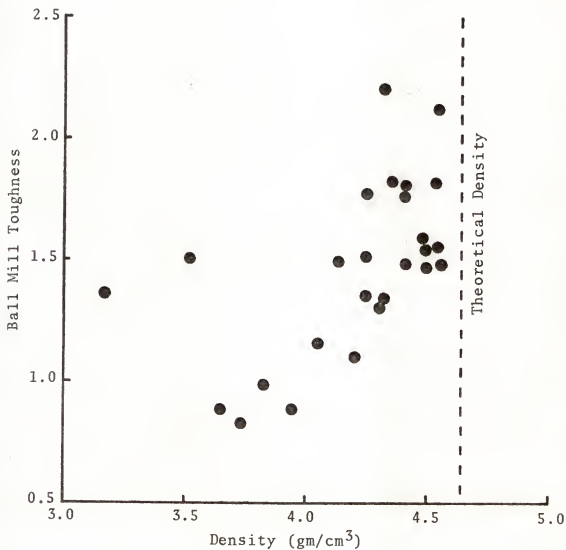


Figure 84. Toughness as a function of density for 42 wt% ZrO₂-58 wt% Al₂O₃. Theoretical density assumes no solid solution.

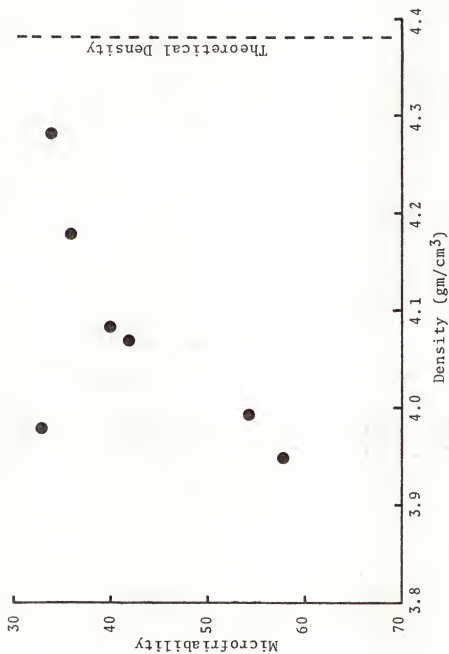


Figure 85. Microfriability as a function of density for 25 wt% ZrO₂-75 wt% Al₂O₃. Theoretical density assumes no solid solution.

X-ray

Powder diffraction patterns show the alumina-zirconia materials studied to consist of α -alumina (corundum crystal structure) and monoclinic zirconia. Some zirconia was found to be in the tetragonal or cubic form. Figure 86 shows the percentage of the stabilized zirconia for the 42 and 25 wt% ZrO_2 cases. Figure 86 shows the amount of stabilization does not depend on quench rate. No detectable shift in powder pattern line spacings was found, indicating no solid solution in the alumina or the zirconia.

Impurities can stabilize zirconia in the tetragonal or cubic phase form. The effects of the additions of CaO , TiO_2 , Cr_2O_3 and V_2O_5 are shown in Figures 87 and 88. CaO stabilizes the cubic modification while TiO_2 shows no effect. Cr_2O_3 and V_2O_5 have a slight stabilizing effect at large concentrations.

No correlations were found between the percent of stabilized zirconia and the geometric microstructure nor were any found with the friability.

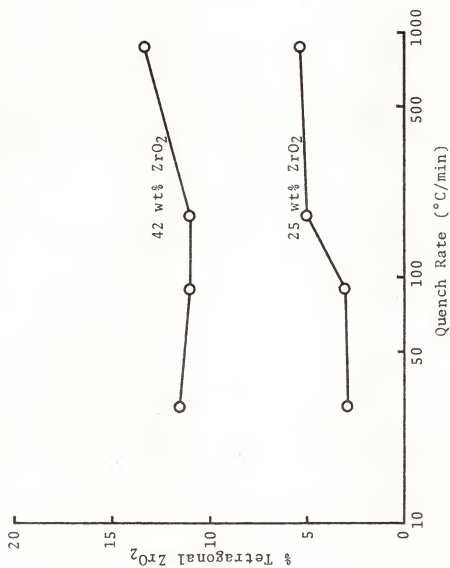


Figure 86. Percent stabilized zirconia as a function of quench rate for 25 wt% ZrO_2 -75 wt% Al_2O_3 and 42 wt% ZrO_2 -58 wt% Al_2O_3 .

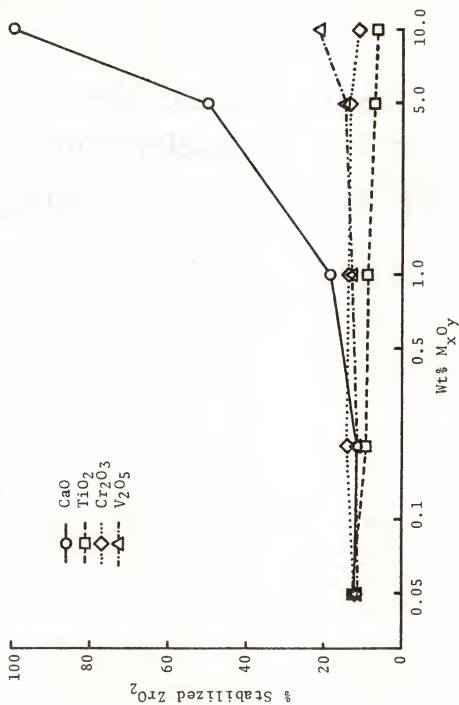


Figure 87. Percent stabilized zirconia dependence on impurities for 42 wt% ZrO_2 -58 wt% Al_2O_3 .

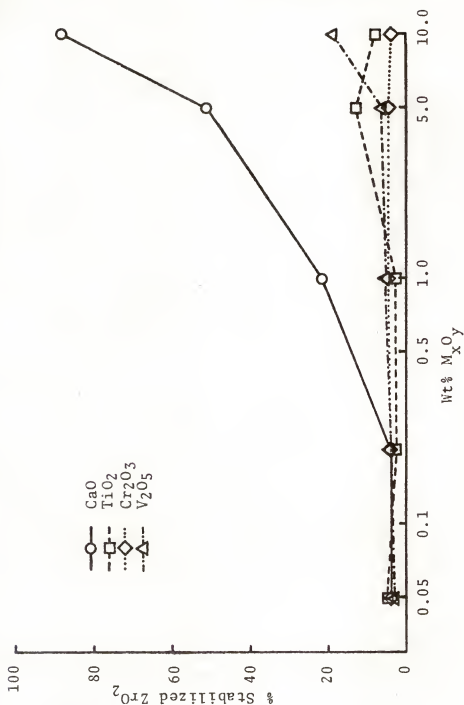


Figure 88. Percent stabilized zirconia dependence on impurities for 25 wt% ZrO_2 -75 wt% Al_2O_3 .

DISCUSSION

Microhardness

Microhardness has been related to friability in a general way by Ueltz [37] and his findings are reproduced in Figure 89. He finds the hardest grains are the most friable while the softer grains are the toughest. Since microhardness is a measure of strength, this shows the general trend for most ceramic materials. Brecker and others [38] have obtained nearly identical results using the same materials as did Ueltz. The friability numbers reported in Figure 89 were obtained using the ASA Ball Mill Friability Index (ASA B74.8-1965). These friability numbers are not directly comparable to those obtained in this study.

Figures 10 and 11 show the variation of microhardness with composition. It has been shown [36] that at a given composition the microhardness can vary with processing variables. Microhardness numbers obtained in this study showed the laboratory samples to have consistently higher hardness than the commercial samples studied. Microfriability tests on some commercial 25 wt% ZrO_2 materials showed friabilities in about the middle of the range obtained for the laboratory materials. Microfriabilities for commercial 42 wt% ZrO_2 materials were slightly higher on the average than the

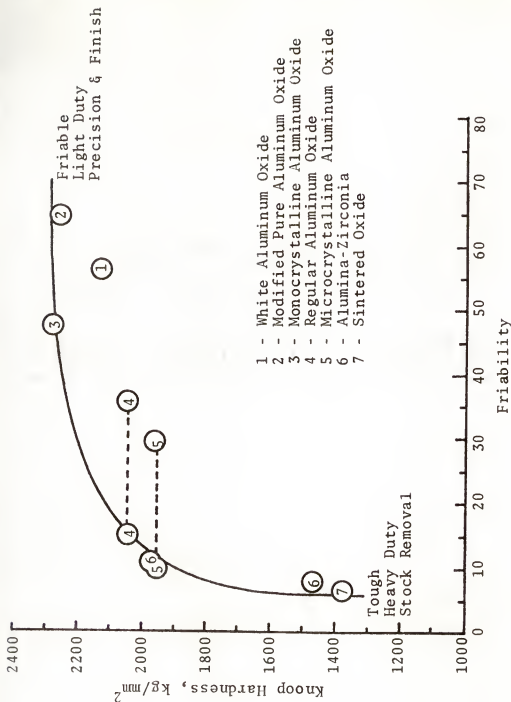


Figure 89. Hardness versus friability for various abrasive grains (12-grit size), after Ueltz [37].

laboratory materials. The variations in friability obtained at a given composition were greater than the variations in hardness (on the order of 200% compared to 10%).

The large variations in friability for alumina-zirconia materials obtained in this study indicate that the alumina-zirconia materials do not fit the plot of Figure 89. Removing the alumina-zirconia from that plot leaves only the alumina abrasives, single phase systems. The indication of decreasing strength with increasing toughness is one generally observed in single phase homogeneous ceramics.

Alumina-zirconia abrasive is tougher than pure alumina abrasives but this increase in toughness is not necessarily accompanied by a decrease in strength. The microhardness data for arc-cast materials in Figures 10 and 11 indicate that the microhardness (or strength) changes little between pure alumina and about 25 wt% ZrO_2 . Between 25 wt% ZrO_2 and pure zirconia the microhardness decreases linearly with increasing zirconia. Tensile strength data by Brecker and others [38] show alumina-zirconia abrasives to be stronger in general than most all pure alumina abrasives. They also show the 25 wt% ZrO_2 composition to be the strongest alumina-zirconia composition and strongest of all alumina abrasives excepting sintered alumina.

The friability of the 25 wt% ZrO_2 is generally a little less than the 42 wt% ZrO_2 . This, combined with the high strength of the 25 wt% ZrO_2 material, shows why it performs better in heavy duty grinding operations.

Microstructure

Materials of different compositions and different preparation procedures have been investigated with respect to V_V^α and $S_V^{\alpha\beta}$ and their effects on the results of tests on single abrasive grains [39,40]. It was found that a V_V^α value of approximately 0.7 and the highest $S_V^{\alpha\beta}$ attained ($\approx 6000 \text{ cm}^{-1}$) gave the toughest abrasive grain.

The data obtained in this study show that the microstructure of the alumina-zirconia system can be controlled and that the microstructure controls the friability. The effects of composition on the microstructure were as expected from the phase diagram. The composition giving the toughest abrasive grain is 25 wt% ZrO_2 . This is slightly greater than the composition where $S_V^{\alpha\beta}$ and $M_V^{\alpha\beta}$ appear to go through a maximum. If the connectivity of the α phase had been measured, it probably would have shown an important relationship to the maximum values of $S_V^{\alpha\beta}$ and $M_V^{\alpha\beta}$. It also might account for the microhardness being essentially constant between 0 and 25 wt% ZrO_2 . The α phase probably becomes completely connected just below the 25 wt% ZrO_2 value, and as the β phase becomes disconnected the toughness decreases to the pure arc-cast alumina value. Also, the connectivity of the α phase between 0 and 25 wt% ZrO_2 would account for the constant microhardness since the hardness would just be that of the connected alumina phase.

At the 25 wt% ZrO_2 composition, the microstructure can be controlled by the quench rate. The faster quench rates

are probably associated with greater amounts of undercooling. Faster quench rates give larger $S_V^{\alpha\beta}$ and larger $M_V^{\alpha\beta}$ values. $M_V^{\alpha\beta}$ and $|M_V^{\alpha\beta}|$ have nearly the same numerical values since the T_A^+ counts were much larger than the T_A^- counts. So no new information is obtained in the $|M_V^{\alpha\beta}|$ parameter that is not already in the $M_V^{\alpha\beta}$ parameter. Since V_V^α is essentially constant, the $\bar{\lambda}$ parameter contains no new information not already contained in $S_V^{\alpha\beta}$. It does provide a better frame of reference for viewing the microstructure since it has units of length, however.

Similarly, for the series with 42 wt% ZrO_2 , $M_V^{\gamma\omega}$ and $|M_V^{\gamma\omega}|$ contain the same information and $S_V^{\gamma\omega}$ and $\bar{\lambda}^\gamma$ contain the same since V_V^γ is constant.

In both the α - β and γ - ω cases mentioned above, all the information obtained on the microstructure is in S_V and M_V since V_V is constant. $\bar{\lambda}$ indicates the scale of the microstructure through S_V while M_V contains shape information. This shape information is most easily obtainable from the $\overline{H\lambda}$ parameter. Using a cylindrical model provides one of the simplest means to calculate $\overline{H\lambda}$. For a cylinder of height h and radius r the following relations are true:

$$V = \pi r^2 h \quad (9)$$

$$S = 2\pi r^2 + 2\pi rh \quad (10)$$

$$M = \pi h + 2\pi^2 r \quad (11)$$

Applying Equation 8 gives $\overline{H\lambda}$ as

$$\overline{H\lambda} = \frac{\frac{h}{r}(\frac{h}{r} + 2\pi)}{(1 + \frac{h}{r})^2} \quad (12)$$

Figure 90 is a plot of $\overline{H\lambda}$ versus h/r . Close examination of the cylindrical model reveals its versatility. For $r \gg h$ or $h/r \ll 1$ the cylinder reduces to a thin disc. A thin disc is a good representation of a plate. $\overline{H\lambda}$ in this case becomes

$$(\overline{H\lambda})_{\text{plate}} \cong 2\pi \frac{h}{r} \quad (13)$$

From Figure 90 it can be seen that small values of $\overline{H\lambda}$ give rise to a plate shape. For the other extreme, $h \gg r$ or $h/r \gg 1$, the cylinder becomes a rod and $\overline{H\lambda}$ becomes

$$(\overline{H\lambda})_{\text{rod}} \cong 1 \quad (14)$$

By evaluating the first derivative of $\overline{H\lambda}$ at 0 the maximum is found to occur at

$$\left(\frac{h}{r}\right)_{\text{max}} = \frac{\pi}{\pi-1} \cong 1.46 \quad (15)$$

and

$$(\overline{H\lambda})_{\text{max}} = \frac{\pi^2}{2\pi-1} \cong 1.87$$

So by this model plates will have $\overline{H\lambda}$ values less than about 0.5 and rods will have values from 1.0 to about 1.5.

While the cylindrical model is simple, it does model two important extremes quite well and provides good ideas of $\overline{H\lambda}$ values for other shapes as long as they have closed surfaces convex (or concave) everywhere (excludes any surfaces containing elements of saddle surface). It is worthy to note that

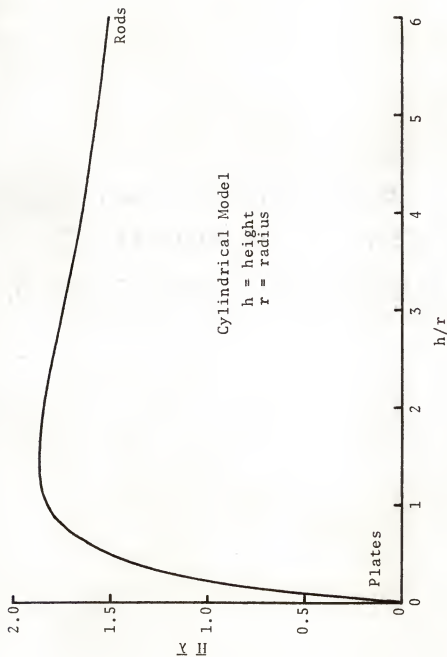


Figure 90. Shape factor for cylinder model as a function of height/radius.

values of $\overline{H\lambda}$ of 1.0 to 1.5 could not only indicate a rod shape but also indicate shapes where $h \approx r$.

Models for simple closed surfaces which eliminate the corners in the cylindrical model, e.g., ellipsoids of revolution [41], give plots similar to Figure 90 and offer no advantage considering the statistical accuracy of the counts leading to $\overline{H\lambda}$. The ellipsoid of revolution model generally shows a lower value for $(\overline{H\lambda})_{\max}$, slightly larger than a sphere where $(\overline{H\lambda})_{\text{sphere}} = 4/3$.

Figures 23, 38 and 55 all have $\overline{H^{\gamma\omega}\lambda^{\gamma}}$ values for different samples. With the exception of a few points, all the $\overline{H^{\gamma\omega}\lambda^{\gamma}}$ values fall between 0.5 and 0.8. This is consistent with values obtained for other samples not reported in this study. Qualitative observation of the γ - ω microstructure shows rods and plates of γ in the ω matrix. The values of $\overline{H^{\gamma\omega}\lambda^{\gamma}}$ obtained indicate a mixture of rods and plates with neither one predominating over the other.

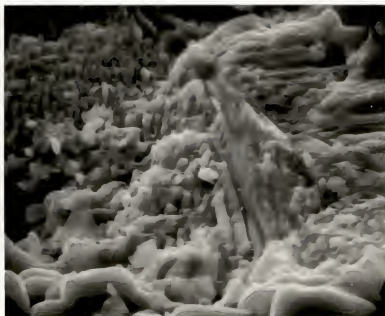
The shape factor remains relatively constant for samples of 42 wt% ZrO_2 . Thus the shape of the γ phase dispersion is independent of processing variables and independent of small chemical additions with a few exceptions. This implies that the $S_v^{\gamma\omega}$ parameter is the most important parameter with which to correlate processing and friability data. Generally, any processing change which decreases the scale in the γ - ω case will decrease the friability (neglecting other effects of impurities).

Figures 31 and 46 reflect $\bar{H}^{\alpha\beta}\bar{\lambda}^{\alpha}$ values from different samples. Excepting a couple of samples with large amounts of impurity additions, all $\bar{H}^{\alpha\beta}\bar{\lambda}^{\alpha}$ values fall between 0.9 and 1.1. Since observation shows the α phase is not present as long rods, then it must be present in shapes best described by the cylindrical model when $h \cong r$. As in the γ - ω case, $S_V^{\alpha\beta}$ is the parameter which best describes the changes in the microstructure observed for samples in this study.

The single most important parameter describing the microstructure in either the α - β or the γ - ω cases is the mean phase intercept, the scale factor. Since the shapes remain relatively constant, the change in M_V values reported merely reflects the change in scale of the microstructure.

The fracture surface of Figure 91 is from a 42 wt% ZrO_2 sample. It illustrates why $S_V^{\gamma\omega}$ controls the friability. The plane of the fracture surfaces tends to be the plane of the γ - ω interface. This is consistent with the theories of Gupta [31] that the weakest part of ceramic composites is the interface between the dissimilar phases. Since the fracture plane is along the alumina-zirconia interface, it must be weaker than either the zirconia or alumina phases themselves. The large amount of surface created upon fracture increases the energy required to propagate the crack and results in a tougher grain than either pure alumina or pure zirconia.

The fracture surfaces observed in this study were very similar to those observed by Hulse [42] for Y_2O_3 stabilized zirconia-alumina eutectic at 1500°C.



5500X

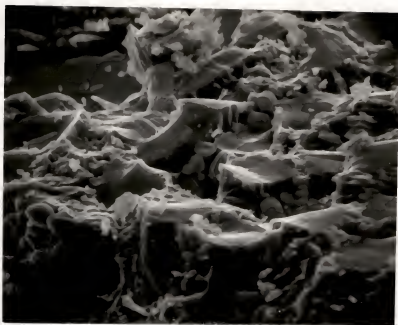
Figure 91. Scanning electron microscope fractograph of eutectic composition cast alumina-zirconia.

Most porosity in the γ - ω case was observed to be shrinkage cavities with occasional gas bubbles depending on the fabrication technique. A very small fraction of the porosity was observed to occur at colony boundaries and in particular at colony edges. For the few samples checked with P_p counts, this type of porosity occupied less than 1% of the total volume, generally on the order of 0.1%. If anything, these estimates are probably high since some rounding of the edge of the porosity at the sectioning plane resulted from the polishing techniques employed.

It is unlikely that the porosity at the colony edges acts as crack initiation points. For these abrasive grains, cracks most certainly initiate at surface flaws on the grain itself. No evidence was found in this study that the crack plane preferred traveling through these areas of porosity. No correlation between friability and colony size or colony surface area could be deduced from the data obtained. Only for very porous samples was the crack front observed to prefer traveling through the porosity.

The same observations with respect to porosity were made in the case of 25 wt% ZrO_2 and all materials on the alumina side of the eutectic composition excepting compositions very near pure alumina. Compositions near pure alumina began to assume the columnar grain shape of pure fusion cast alumina. Fracture surfaces become smoother.

Figure 92 shows a typical fracture surface for a 25 wt% ZrO_2 material. The crack propagates through the supporting



2100X

Figure 92. Scanning electron microscope fractograph of cast 25 wt% ZrO_2 -75 wt% Al_2O_3 .

matrix the same way it propagated in the 42 wt% ZrO_2 case, Figure 91. When the crack front reaches the stronger primary alumina grains, it prefers to take the longer path around the grain since an increase in stress level at the crack tip is required to advance the crack tip through the primary alumina grain. Evidence of this can be seen by the number of primary alumina grains "sticking out" of the fracture plane. The fracture plane itself is very tortuous as in the 42 wt% ZrO_2 case.

Three factors control the strength of composite materials according to Lange [32]--fracture energy, elastic modulus and crack size. The fracture mechanics approach states that the strength of a material will be proportional to the square root of the product of fracture energy and elastic modulus and inversely proportional to the square root of the crack size. These three factors are governed by five composite parameters: (1) the particle size of the dispersed phase, (2) its volume fraction, (3) the degree of interfacial bonding, (4) the modular ratio, and (5) the differential thermal expansion of the phases.

The greatest influence of the dispersed phase is to increase the crack size. Crack size can be minimized, thereby optimizing the composites' strength by making the composite with a small particle size dispersion. A large fracture energy is also desirable for optimum strength. Data from different investigations show that a large particle size dispersion results in the largest fracture energy for a given

composite composition [43-47]. Although larger particle size dispersions result in larger fracture energies, they also are more effective crack precursors and form larger cracks. An increased fracture energy and an increased crack size are competitive strength-controlling factors; a compromise with regard to particle size must be made to obtain the optimum composite strength at a given volume fraction.

The alumina-zirconia composite is stronger and tougher than pure fusion cast alumina. The crack size is larger, which increases the fracture energy. In most materials examined in this study, these competitive strength-controlling factors gave a net increase in the strength of the alumina-zirconia composite.

The two cases of composite systems studied can be examined separately with respect to the effects of the five composite parameters. In the case of the eutectic composition, $\gamma-\omega$, the volume fraction of the dispersed phase, the zirconia, is fixed. The particle size as measured by the mean phase intercept, $\bar{\lambda}^Y$, can be varied by controlling processing variables. Larger $\bar{\lambda}^Y$ means greater crack size and larger fracture energy. The strength has not been quantitatively measured for all the materials included in this study so the optimum $\bar{\lambda}^Y$ cannot be determined. It was suspected that a small $\bar{\lambda}^Y$ value would give the combination of crack size and fracture energy which optimizes the strength. The toughness of the $\gamma-\omega$ material was measured quantitatively and does increase with decreasing $\bar{\lambda}^Y$. The elastic modulus depends primarily on the

volume fraction of the dispersed phase and the modular ratio of the dispersed phase and the matrix phase and these are constant. The elastic modulus also depends indirectly on particle size, interfacial bonding and differential thermal expansion due to the possibility of crack formation during cooling. The interfacial bonding between the alumina and the zirconia is relatively weak as was seen in Figure 91. The crack front propagates along this boundary, giving rise to larger crack sizes and higher fracture energies. The bonding is strong enough, though, to create a tough ceramic. The difference in the thermal expansion of alumina and zirconia is significant but no cracks were observed in the materials fabricated. There could be cracks formed, though, which have sizes below the limits of detectability. Smaller particle size dispersions, smaller $\bar{\lambda}^Y$, would lead to smaller crack sizes which would give stronger materials. In glass matrix systems [48], it has been found that cracks do not form with small particle size dispersions and strengthening could be obtained despite large differences in thermal expansion. The same conclusion could be drawn about the alumina-zirconia system.

In the α - β composite case, many of the same arguments presented above can be presented again. The volume fraction of the dispersed phase, the primary alumina dendrites, can be varied and the maximum strength [38] occurs at volume fractions of about 0.7 which is the 25 wt% ZrO_2 composition. The toughest material also occurs at this composition. The

strongest and toughest materials are those with small $\bar{\lambda}^{\gamma}$ values. The interfacial bonding between the primary alumina and the matrix is very good, being essentially an alumina-alumina bond. The plane of fracture is along the alumina-zirconia boundary in the matrix and preferentially around the dispersed primary alumina. The increased strength of the α - β case and, in particular, the 25 wt% ZrO_2 composition arises from an increase in the fracture energy and most probably an increase in the elastic modulus over the γ - ω case, although the elastic modulus values have never been quantitatively measured. A tougher ceramic is also obtained due to the arresting of propagating cracks through the material.

Zirconia Stabilization

The stabilization of zirconia which did occur was probably due mainly to an impurity effect. It appears unlikely that it was due to a size effect. If it had been due to a size effect, then a small percentage of the zirconia would have been present in crystallite sizes on the order of 100-200 Å [27-29]. It would be expected that as the scale of the system decreased, the percentage of the zirconia in this small size range would also increase and thus the amount of stabilized zirconia should increase. This was not observed in the quench rate experiments. The amount of stabilized zirconia was independent of quench rate.

Experiments with different starting raw materials and different fabrication techniques showed variations in the

amount of stabilized zirconia although the amount remained small. The differences due to different raw materials could obviously be due to impurities. The differences due to different fabrication techniques could also be due to impurities introduced by the techniques. Laboratory samples fabricated for testing probably had various amounts of oxides of tungsten and molybdenum. Commercial samples had a fairly large range of stabilization which again could probably be traced to impurities.

No correlations between the amount of stabilized zirconia and microstructure or friability were observed.

Impurities

Impurities were found to cause variations in the microstructure and variations in the friability. The effects of impurities on the friability beyond the effects produced by microstructural changes are of interest for the fabrication of abrasive grains. For the γ - ω case TiO_2 , Cr_2O_3 and V_2O_5 gave less friable material than the microstructural changes would predict. For the TiO_2 case, x-ray diffraction analysis showed small amounts of Al_2TiO_5 were formed at the higher TiO_2 concentrations. The Al_2TiO_5 could have been present at the grain boundaries of other compositions, too, in amounts too small to detect. Al_2TiO_5 is a softer material than Al_2O_3 or ZrO_2 , which would give an increase in toughness. Similarly, for V_2O_5 additions, AlVO_4 was formed giving a decrease in strength and an increase in toughness. AlVO_4 is a softer

phase, also. Cr_2O_3 is isomorphous with Al_2O_3 and it has been shown that solid solution of Cr_2O_3 in Al_2O_3 results in an increase in strength [49-50]. This same increase in strength probably occurred in the alumina-zirconia materials. The increase in toughness observed for Cr_2O_3 additions could have been due to the release of tension in the Al_2O_3 lattice caused by the larger Cr^{+3} ions in solution. According to Belon and others [50], a similar argument might be proposed for the TiO_2 and V_2O_5 cases.

In the α - β case, only Cr_2O_3 gave an abrasive less friable than the microstructural changes predicted. The effects of the tougher matrix phases in the TiO_2 and V_2O_5 cases were balanced apparently by the increase in strength of the primary alumina due to solid solution [50] leading to a more brittle α -phase which gave a decrease in toughness. Fracture surfaces seem to indicate a less tough primary alumina since the fracture plane no longer appears to circumvent the primary alumina but continues uninterrupted through it. This was not observed to happen for the Cr_2O_3 additions.

The large increases in friability for CaO additions beyond small fractional percentages was due to $\text{CaO-Al}_2\text{O}_3$ glass formation. The composition of the last liquid to freeze [51] and the fast quench rates involved in sample preparations were sufficient to produce the glassy phase.

Friability and Grain Shape

This study has shown that microstructure controls the friability. Impurities can also control the friability beyond the microstructural changes they produce. There are other factors which control the friability of a material which have not been examined in this study.

Two factors of importance are the size and shape of the abrasive grain. The size effect is generally much smaller than the shape effect. All directly comparable results in this study were obtained using the same size grains. Ueltz has shown the effect of shape on the friability of alumina abrasives. The dependence on shape was the reason the grains were tumbled and tumbled for this study as mentioned in a previous section. The effect of shape has been minimized to allow observation of other factors controlling friability.

CONCLUSIONS

The conclusions reached in this study can be summarized as follows:

1. The microstructure of the alumina-zirconia system can be adequately described by the techniques of quantitative microscopy.
2. The microstructure of the alumina-zirconia system can be controlled by controlling the processing variables.
3. The quench rate was the most important processing variable affecting the microstructure of the alumina-zirconia materials studied.
4. The microstructure controls the friability of alumina-zirconia materials.
5. The scale of the microstructure, $\bar{\lambda}$, is the feature of the microstructure which controls the friability.
6. The increased toughness and strength of the alumina-zirconia materials studied comes from arrested crack propagation and increased fracture energies.
7. Alumina does not stabilize zirconia in the cubic or tetragonal phase form.
8. Impurities can affect the mechanical properties of alumina-zirconia beyond the effects produced by microstructural changes. Increases in strength and increases in toughness can be produced by impurities.

9. The best abrasive material in the alumina-zirconia system for heavy duty stock removal is a composition of about 25 wt% ZrO_2 and with a microstructure having the smallest scale factor possible.

FUTURE WORK

A need exists for more work on the microstructural aspects of the alumina-zirconia system. For abrasive grain applications, mechanical testing must be extended beyond friability testing. More tensile strength data could be useful and attritious wear measurements are needed. Actual grinding processes should be employed and grinding ratios calculated. Tests more related to actual grinding operations would have to be performed for each workpiece under consideration.

The fabrication procedures could be expanded beyond those used in this study. The effects of going from a laboratory scale fabrication to a commercial production scale should be investigated.

The effects of impurities need more investigation. The number of impurities must be expanded to include more of those commonly found in commercial materials, in particular, Fe_2O_3 , SiO_2 , Na_2O , sulfides, chlorides and carbides. Combinations of impurities also need to be studied.

The techniques used in this study of the alumina-zirconia system could be applied to other composite materials. The relation between microstructure and mechanical properties need not be concerned solely with properties of abrasives but can be extended to materials for other applications.

REFERENCES

1. Quantitative Microscopy, ed. by R.T. DeHoff and F.N. Rhines, McGraw-Hill: New York (1968).
2. E.E. Underwood, Quantitative Stereology, Addison-Wesley: Reading, Mass. (1970).
3. J.E. Hilliard and J.W. Cahn, "An Evaluation of Procedures in Quantitative Metallography for Volume Fraction Analysis," Trans. Met. Soc. AIME 221, 344-52 (1961).
4. C.S. Smith and L. Guttman, "Measurement of Internal Boundaries in Three Dimensional Structures by Random Sectioning," Trans. Met. Soc. AIME 197, 81-7 (1953).
5. R.T. DeHoff, "The Quantitative Estimation of Mean Surface Curvature," Trans. Met. Soc. AIME 239, 617-21 (1967).
6. R.L. Fullman, "Measurement of Particle Sizes in Opaque Bodies," Trans. Met. Soc. AIME 197, 447-52 (1953).
7. J.W. Cahn, "The Significance of Average Mean Curvature and Its Determination by Quantitative Metallography," Trans. Met. Soc. AIME 239, 610-16 (1967).
8. A.M. Alper, "Microstructures Developed from Fusion Casting," in Ceramic Microstructures, ed. by R.M. Fulrath and J.A. Pask, Wiley: New York (1968), p. 776.
9. A.M. Alper, Phase Diagrams, Vol. II, Academic Press: New York (1970), pp. 127-30.
10. G. Pahlitzsch and K1.H. Thormahlen, "Grinding With Alloyed and Unalloyed Corundum," in New Developments in Grinding, ed. by M.C. Shaw, Carnegie Press: Pittsburgh, Penn. (1972), pp. 127-41.
11. L. Coes, Jr., Abrasives, Springer-Verlag: New York (1971), pp. 65, 128.
12. L.E. Erikson and F.S. Gibbs, "Analysis of Foundry Floorstand Grinding," Mod. Cast. 63 [6], 55-6 (1973).

13. T. Matsuo and E. Oshima, "Wear and Micro-Chipping of Single Abrasive Grains," presented to 1973 C.I.R.P. General Assembly, Bled, Yugoslavia (Aug., 1973).
14. G.K. Lal and M.C. Shaw, "Wear of Single Abrasive Grains in Fine Grinding," in New Developments in Grinding, ed. by M.C. Shaw, Carnegie Press: Pittsburgh, Penn. (1972), pp. 107-26.
15. G.K. Lal, T. Matsuo and M.C. Shaw, "An Investigation of the Wear of Abrasive Grains by Rubbing on Ferrous and Non-Ferrous Surfaces," Wear 24 [3], 279-93 (1973).
16. G.K. Lal and M.C. Shaw, "On the Attritious Wear of Abrasive Grains," Wear 25 [2], 255-69 (1973).
17. H. von Wartenberg, H. Linde and R. Jung, Z. Anorg. Allg. Chem. 176, 349-63 (1928).
18. H. von Wartenberg and H.S. Reusch, Z. Anorg. Allg. Chem. 207, 18 (1932).
19. Von G. Cevalles, "Phase-Equilibrium Diagram of $\text{Al}_2\text{O}_3\text{-ZrO}_2$ and Examination of a New Phase ($-\text{Al}_2\text{O}_3$)," Ber. Deut. Keram. Ges. 45, 216-19 (1968).
20. F. Schmid and D. Viechnicki, "Ceramic Eutectics," in Advanced Materials: Composites and Carbon, compiled by J.D. Buckley, American Ceramic Society: Columbus, Ohio (1972), pp. 97-104.
21. B. Chalmers, Principles of Solidification, Wiley: New York (1964), p. 207.
22. B.E. Sundquist and L.F. Mondolfo, "Heterogeneous Nucleation in the Liquid-to-Solid Transformation in Alloys," Trans. Met. Soc. AIME 221, 157-64 (1961).
23. N.J. Parrat, Fibre-Reinforced Materials Technology, Van Nostrand: New York (1972), pp. 111-17.
24. B.C. Weber, "An Annotated Bibliography of Research on the Structural and Physical Properties of Zirconia," Aerospace Research Lab Report ARL 64-205 (1964).
25. F. Schmid and D. Viechnicki, "Oriented Eutectic Microstructures in the System $\text{Al}_2\text{O}_3/\text{ZrO}_2$," J. Mat. Sci. 5, 470-73 (1970).
26. A.B. Andreeva, A.I. Leonov and E.K. Keller, "A Highly Refractory Material Based on Zirconia Stabilized with Yttrium and Aluminum Oxides," Ogneupory 4, 42-5 (1973).

27. A. Krauth and H. Meyer, "Crystal Modifications Produced by Chilling and Their Growth Rate in Systems Containing Zirconium Dioxide," Ber. Dtsch. Keram. Ges. 42, 61-72 (1965).
28. R.C. Garvie, "The Occurrence of Metastable Tetragonal Zirconia as a Crystallite Size Effect," J. Phys. Chem., 69 [4], 1238-43 (1965).
29. J.E. Bailey, D. Lewis, Z.M. Librant and L.J. Porter, "Phase Transformations in Milled Zirconia," Trans. J. Brit. Ceram. Soc. 71 [1], 25-30 (1972).
30. Von H.W. Hennicke and H. Vaupel, "The Stabilization of Zirconium Oxide with Aluminum Oxide," Tonid. Ztg. 94 [2], 45-50 (1970).
31. T.K. Gupta, "A Qualitative Model for the Development of Tough Ceramics," J. Mat. Sci. 9 [10], 1585-89 (1974).
32. F.F. Lange, "Strength Behavior of Brittle Matrix, Particulate Composites," in Fracture and Fatigue of Composites, ed. by L.J. Broutman and R.H. Krock, Academic Press: New York (1973).
33. R.W. Davidge and A.G. Evans, "The Strength of Ceramics," Mater. Sci. Eng. 6 [5], 281-98 (1970).
34. T.K. Gupta, "Strength Degradation and Crack Propagation in Thermally Shocked Al_2O_3 ," J. Amer. Ceram. Soc. 55 [5], 249-53 (1972).
35. R.C. Garvie and P.S. Nicholson, "Phase Analysis in Zirconia Systems," J. Amer. Ceram. Soc. 55 [6], 303-5 (1972).
36. R.E. Shepler, N.R. Hirji, G. Walther, T.P. Oxford, D.M. Sanders, R.E. Loehman and E.D. Whitney, Ultrahard Grinding Materials Research, Final Report NSF Grant GK-29362, Engineering and Industrial Experiment Station, University of Florida, Gainesville, Fla. 1973.
37. H.F. Ueltz, "Abrasive Grains - Past, Present and Future," in New Developments in Grinding, ed. by M.C. Shaw, Carnegie Press: Pittsburgh, Penn. (1972), p. 50.
38. J.N. Brecker, R. Komanduri, C. Liatsos and M.C. Shaw, Ultra Hard Grinding Materials Investigation, First Year Report NSF Grant GK-29361, Mechanical Engineering, Carnegie-Mellon University, Pittsburgh, Penn. (1972).

39. E.D. Whitney and R.E. Shepler, "Ceramics in Abrasive Processes," in Surfaces and Interfaces of Glass and Ceramics, ed. by V.D. Frechette, W.C. Lacourse and V.L. Burdick, Plenum Press: New York (1974), pp. 167-78.
40. E.D. Whitney and R.E. Shepler, "Quantitative Microscopy of Alumina-Zirconia Abrasives," to be publ. in Proceedings of International Conference on Production Technology, Melbourne, Australia (1974).
41. R.T. DeHoff, "The Determination of the Geometric Properties of Aggregates of Constant Size Particles from Counting Measurements Made on Random Plane Sections," Trans. AIME 230, 764-69 (1964).
42. C.O. Hulse and J.A. Batt, "Fracture Behavior of Directionally Solidified $\text{Al}_2\text{O}_3\text{-ZrO}_2$ (Y_2O_3) Eutectic," paper presented at the 75th Annual Meeting of the American Ceramic Society, Cincinnati, Ohio (April, 1973).
43. F.F. Lange and K.C. Radford, "Fracture Energy of an Epoxy Composite System," J. Mat. Sci. 6, 1197-1203 (1971).
44. D.P.H. Hasselman and R.M. Fulrath, "Proposed Fracture Theory of a Dispersion-Strengthened Glass-Crystal Composite," J. Amer. Ceram. Soc. 49, 68-72 (1966).
45. W.J. Frey and J.D. MacKenzie, "Mechanical Properties of Selected Glass-Crystal Composites," J. Mat. Sci. 2, 124-30 (1967).
46. F.F. Lange, "Relation Between Strength, Fracture Energy and Microstructure for Hot-Pressed Silicon Nitride," Scientific Paper 72-9D4-SERAM-P1 (1972).
47. K.C. Radford, "The Mechanical Properties of an Epoxy Resin with a Second Phase Dispersion," J. Mat. Sci. 6, 1286-91 (1971).
48. D.B. Binns, Science of Ceramics 1, ed. by G.H. Stewart, Academic Press: London (1962), pp. 315-35.
49. R.C. Bradt, " Cr_2O_3 Solid Solution Hardening of Al_2O_3 ," J. Amer. Ceram. Soc. 50 [1], 54-5 (1967).
50. L. Belon, H. Forestier and Y. Bigot, "The Hardness of Some Solid Solutions of Alumina," Proc. Symp. Brit. Ceram. Res. Ass. 1967 [4], 203-11 (1968).
51. H. Rawson, Inorganic Glass-Forming Systems, Academic Press: New York (1967), pp. 28, 199-200.

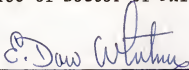
BIOGRAPHICAL SKETCH

Robert Eugene Shepler was born March 29, 1945, in Valley City, North Dakota. He attended St. John's University, Collegeville, Minnesota, from 1963 to 1965. He then attended the University of North Dakota, Grand Forks, North Dakota, from 1965 to 1967 and received a Bachelor of Science degree. In 1967 he entered graduate school at the University of North Dakota and received a Master of Science degree in 1969. From 1969 to 1971 he served in the United States Army.

In 1971 he entered the Graduate School in the Department of Metallurgical and Materials Engineering (since then renamed Department of Materials Science and Engineering) at the University of Florida. In 1975 he received the degree of Doctor of Philosophy.

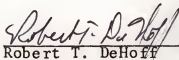
The author is a member of the American Society for Metals, American Institute of Mining, Metallurgical and Petroleum Engineers, American Ceramic Society, Alpha Sigma Mu and Sigma Xi.

I certify that I have read this study and that in my opinion it conforms to acceptable standards of scholarly presentation and is fully adequate, in scope and quality, as a dissertation for the degree of Doctor of Philosophy.



E. Dow Whitney, Chairman
Associate Professor of
Materials Science and Engineering

I certify that I have read this study and that in my opinion it conforms to acceptable standards of scholarly presentation and is fully adequate, in scope and quality, as a dissertation for the degree of Doctor of Philosophy.



Robert T. DeHoff
Professor of Materials Science
and Engineering

I certify that I have read this study and that in my opinion it conforms to acceptable standards of scholarly presentation and is fully adequate, in scope and quality, as a dissertation for the degree of Doctor of Philosophy.




Larry L. Hench
Professor of Materials Science
and Engineering

I certify that I have read this study and that in my opinion it conforms to acceptable standards of scholarly presentation and is fully adequate, in scope and quality, as a dissertation for the degree of Doctor of Philosophy.



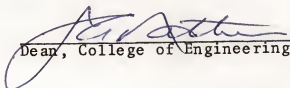
Ronald E. Loehman
Assistant Professor of
Materials Science and Engineering

I certify that I have read this study and that in my opinion it conforms to acceptable standards of scholarly presentation and is fully adequate, in scope and quality, as a dissertation for the degree of Doctor of Philosophy.


James B. Conklin, Jr.
Associate Professor of Physics

This dissertation was submitted to the Graduate Faculty of the College of Engineering and to the Graduate Council, and was accepted as partial fulfillment of the requirements for the degree of Doctor of Philosophy.

June, 1975


Dean, College of Engineering

Dean, Graduate School